Master's Thesis

γ-ray spectroscopy study of $^{11}_{\Lambda}$B and $^{12}_{\Lambda}$C

Tohoku University
Graduate School of Science
Department of Physics

Yue Ma

2006

Abstract

This dissertation mainly explains the preliminary analysis result of the KEK-E566 experiment. The purpose of the present experiment is to investigate the precise structure of ${}^{12}_{\Lambda}$C and ${}^{11}_{\Lambda}$B hypernuclei by γ-ray spectroscopy technique, and to test the universality of the experimentally determined parameters on the strengths of the ΛN spin-dependent interactions, which is based on a shell model calculation in a weak coupling scheme. In particular this experiment enables us to investigate the effect of the ΛNN three body interaction to p-shell hypernuclei. To measure the g-factor of a Λ hyperon in a nucleus is also a goal of the current experiment.

In this experiment, we employed ^{12}C(π^+, K$^+$)${}^{12}_{\Lambda}$C reaction to populate the ${}^{12}_{\Lambda}$C and ${}^{11}_{\Lambda}$B hypernuclei at the KEK-PS K6 beam line. A germanium detector array, Hyperball2, was used in conjunction with the magnetic spectrometer system in the K6 beam line to detect the γ rays emitted from the populated hypernucleus. In the current stage, three γ-ray peaks were confirmed to be emitted from the hypernucleus as:

$$ {}^{11}_{\Lambda}\mathrm{B} : E_\gamma(7/2^+ \rightarrow 5/2^+) = 261.6 \pm 0.24 \ \ \mathrm{keV}, $$

$$ {}^{11}_{\Lambda}\mathrm{B} : E_\gamma(1/2^+ \rightarrow 5/2^+) = 1481.7 \pm 0.7 \ \ \mathrm{keV\ and} $$
$$ {}^{12}_{\Lambda}\mathrm{C} : E_\gamma(1^-_2 \rightarrow 2^-_1) = 2667.3 \pm 2.8 \ \ \mathrm{keV}. $$

A comparison with a theoretical prediction given by Millener shows a deviation of about 200 keV from the experimental value in the case of ${}^{11}_{\Lambda}$B:$(7/2^+ \rightarrow 5/2^+)$ and ${}^{12}_{\Lambda}$C:$(1^-_2 \rightarrow 2^-_1)$.
Another γ-ray peak was found around 180 keV, which is the candidate for the ground state doublet transition of ${}^{12}_{\Lambda}$C$(2^-_1 \rightarrow 1^-_1)$. However, further analysis is necessary before we can draw a conclusion.

Contents

List of Figures

List of Tables

Chapter 1

Introduction

1.1 General Introduction

Hypernuclear physics studies the nuclear systems that contain hyperons: the baryons which consist of strange quarks as well as up and down quarks. The Λ hyperon (Λ for short) is the lightest hyperon. In our current research we mainly focus on the hypernucleus that has a Λ only. The Λ particle was first discovered in an emulsion experiment [1]. It was characterised by its long life time ($\tau \sim 2.6\times10^{-10}$ s) , which is a consequence of quark flavour conservation in the strong interaction. The word *strangeness* was introduced for this reason. The constituents of the Λ can be expressed as $\Lambda(u, d, s)$. The intrinsic properties of the Λ and other nucleons are summarised in Table 1.1. Because

Table 1.1: Intrinsic property of Λ and nucleon

Particle	Mass(MeV/C^2)	Spin	Isospin	Charge	Strangeness
p	938.27	$\frac{1}{2}$	$\frac{1}{2}$	1	0
n	939.56	$\frac{1}{2}$	$-\frac{1}{2}$	0	0
Λ	1115.68	$\frac{1}{2}$	0	0	-1

of similar properties shared by them, they can be regarded as members of the same baryon family. The ultimate goal in the hypernuclear research is to obtain a unified baryon-baryon interaction picture.

The exciting features of hypernuclear physics brought by the presence of a Λ are rich. For instance, the Λ is free from the nucleons' Pauli blocking, which is suffered by normal nuclei, because it has additional strangeness degree of freedom. Consequently, the Λ can go deep into the nuclear core giving the information on the innermost of nucleus. The single particle states of a Λ inside the nucleus observed by spectroscopy experiments were considered as a direct evidence for the existence of the effective nuclear potential [2].

Unlike normal nuclear physics, we can hardly perform Λ-Nucleon scattering experiments because of the difficulty of producing low energy Λ beam. Thus, an alternative way to study the interaction between a Λ and nucleon is necessary. Before 1970s, emulsion experiments played an important role in the research of hypernuclear physics. Because the emulsion experiments detect weak decay products, π^- and/or proton, from the hypernucleus to identify the production of the hyperon, it can provide the ground state information of the hypernucleus. The binding energy of the Λ has been measured accurately in this way, which showed that the nuclear potential depth for a Λ is about two thirds of that for a nucleon [3]. After 1970s, counter experiments became the main stream in the hypernuclear research. For example, the spectroscopy from (K^-, π^-) experiments have revealed the level structure of Λ hypernuclei. In a systematic spectroscopy study with (π^+, K^+) reaction, the correlation between the binding energy of the Λ hyperon and the mass number of the hypernucleus was disclosed. The results were consistent with a square potential well calculation [4][5]. Apart from these successes, the main constraint for the counter experiments is their limited energy resolution. For example, the best energy resolution achieved in hypernuclear reaction spectroscopy was about 1 MeV, which is improved to be several hundred keV recently by introduction of the (e,$e^{'}\mathrm{K}^+$) reaction. On the other hand, energy resolution of γ-ray spectroscopy is a few keV. Thus the γ-ray spectroscopy plays a unique role in complementing the reaction spectroscopy method.

1.2 Λ-Nucleon (ΛN) Interaction

To study the hyperon-nucleon (YN) interaction, the idea of meson exchange force in the normal nuclear physics (NN interaction) is adopted. However, in the YN interaction, the difference in exchanged mesons and their properties make the detailed description quite different from the NN interaction. For example, because of isospin conservation, one pion exchange is forbidden in the ΛN interaction. Consequently, the most probable meson mediating the ΛN interaction is Kaon. Some of the possible processes of interactions are illustrated in Fig. 1.1.

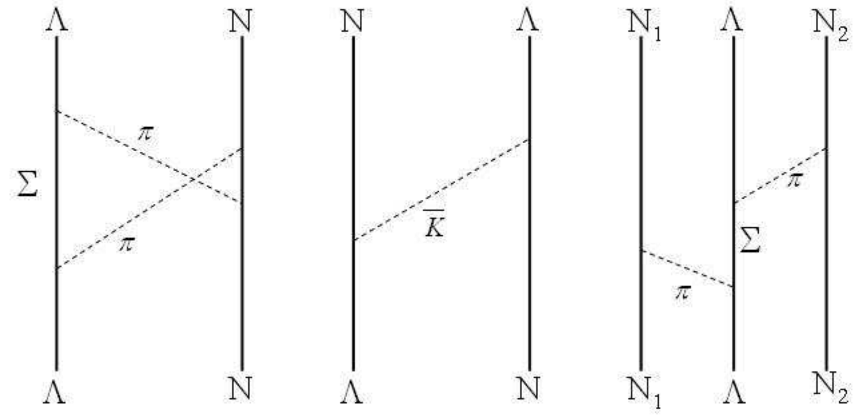

Figure 1.1: Schematic view of Λ -Nucleon (ΛN) interactions [7].

It is practical to connect theories and experiments with so called effective interactions as in normal nuclear physics. The two body interaction between a nucleon and a Λ can be expressed as:

$$\begin{aligned} V_{\Lambda \mathrm{N}}(r) = V_0(r) + V_\sigma(r)\mathbf{s}_\mathrm{N}\cdot\mathbf{s}_\Lambda + V_\Lambda(r)\mathbf{l}_{\mathrm{N}\Lambda}\cdot\mathbf{s}_\Lambda + V_N(r)\mathbf{l}_{\mathrm{N}\Lambda}\cdot\mathbf{s}_\mathrm{N} \\ + V_T(r)\left\{\frac{3(\sigma_\Lambda\cdot\mathbf{r})(\sigma_\mathrm{N}\cdot\mathbf{r})}{r^2} - \sigma_\Lambda\cdot\sigma_\mathrm{N}\right\}, \end{aligned} \tag{1.1}$$

where r means the relative distance between a Λ and a nucleon and $\mathbf{l}_{\mathrm{N}\Lambda}$ stands for the relative orbital angular momentum. The s_N and s_Λ are the spin angular momentum operator of the nuclei and the Λ , respectively. When we consider low-lying levels of p-shell hypernuclei[1], the effective interaction between a Λ in the s-orbit and a nucleon in the p-orbit is important. In this case, level energies are described by five radial integrals corresponding to each of these five terms in Eq. (1.1). The radial integrals of these five terms are introduced as parameters and denoted by $\bar{V}, \Delta, S_\Lambda, S_\mathrm{N}, T$ respectively. For example, $\Delta = \int \phi^*_{\Lambda N}(r)V_\sigma(r)\phi_{\Lambda N}(r)r^2dr$, where $\phi_{\Lambda N}(r)$ is the radial part of the relative wave function between a Λ in the s-orbit and a nucleon in the

[1]The p-shell hypernuclei have a s-orbit Λ hyperon and nucleons that fill up to p-orbit.

p-orbit. The first term in this expression is adjusted to fit the binding energy data. In the following discussion, we will adopt calculations by Millener, which are based on a shell model. The determination of these parameters will be described in the next section. For details, refer to Appendix A.

1.3 Previous Hypernuclear γ-ray Spectroscopy with Hyperball

The hypernuclear γ rays were first measured by NaI counters [8]. However, the application of germanium (Ge) detectors is indispensable with its unparalell energy resolution to study quantitatively the spin-dependent ΛN interactions in the order of a few tens of keV. For this reason, the Hyperball[2] (Ge detector array) project was initiated in 1998. Since then, a series of hypernuclear γ-ray spectroscopy experiments have been performed. The motivation of those experiments is to determine interaction parameters $(\Delta, S_\Lambda, S_\mathrm{N}, T)$ one by one by choosing proper hypernuclei. The main results are listed below:

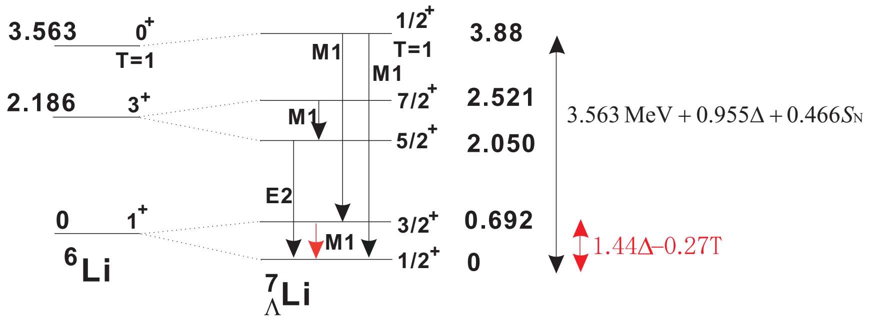

Figure 1.2: $^{7}_{\Lambda}$Li Level Scheme.

The determination of Δ and S_N

In Fig. 1.2, the level scheme of $^{7}_{\Lambda}$Li and the expression for excited energy levels is shown [9]. The ground state doublet spacing is dominated by the Δ term as

$$E_{3/2^+} - E_{1/2^+} = 1.44\Delta - 0.27T, [11]$$

whose experimental value is 0.692 MeV. By assuming a calculated value of T as 0.04 MeV, we may derive $\Delta \sim 0.5$ MeV. Another transition that can be used to derive the parameter is $M1(\frac{1}{2}^+(T=1) \to \frac{1}{2}^+)$. The energy level shift from the ^{6}Li(3^+,1^+) can be attributed to the interaction between the Λ

[2]In the present experiment, we used the second generation Ge detector array, Hyperball2, which will be described in Chapter 2.

and the nuclear core. It can be expressed in terms of the effective interaction as

$$E_{1/2^+}(T=1) - E_{1/2^+} = 3.563 \ \ \text{MeV} + 0.955\Delta + 0.466 S_N = 3.88 \ \ \text{MeV}, [11]$$

which can give a value of S_N as ~ -0.4 MeV. The $E2(\frac{5}{2}^+ \rightarrow \frac{1}{2}^+)$ transition observed in the same experiment also gave a consistent result for the Δ and the S_N.

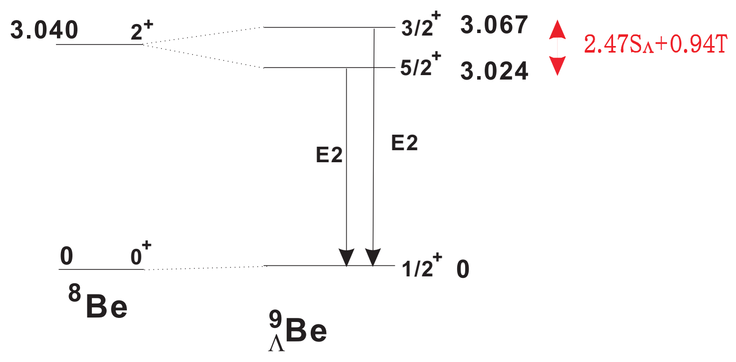

Figure 1.3: ${}^{9}_{\Lambda}$Be Level Scheme.

The determination of S_Λ

To determine S_Λ, the ${}^{9}_{\Lambda}$Be is suitable. Fig. 1.3 shows the level scheme of ${}^{9}_{\Lambda}$Be [12]. The energy spacing between $\frac{3}{2}^+$ and $\frac{5}{2}^+$ is the energy difference between the two $E2$ transitions. This energy spacing, in terms of the effective interaction, can be written as

$$E_{3/2^+} - E_{1/2^+} = 2.47 S_\Lambda + 0.94T = 3.067 \ \ \text{MeV} - 3.024 \ \ \text{MeV}[11].$$

We may then determine the value of S_Λ which is dominant in energy difference of those two E2 transitions. The obtained value of S_Λ is ~ -0.01 MeV.

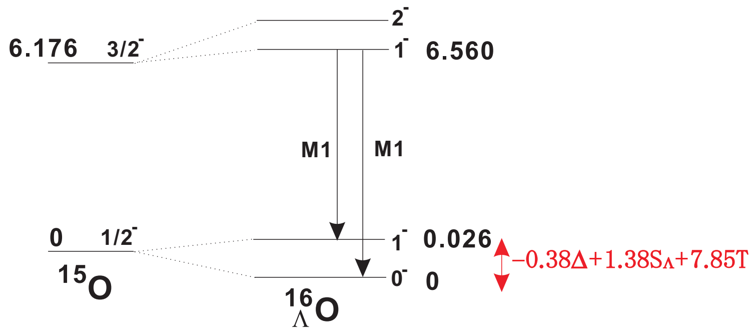

Figure 1.4: ${}^{16}_{\Lambda}$O Level Scheme.

The determination of T

The experimental determination of the T was achieved by the observation of ${}^{16}_{\Lambda}$O as shown in Fig. 1.4 [13]. According to the shell model calculation, the ground state doublet spacing, which was experimentally obtained from the difference of the two $M1$ transitions, can be expressed as

$$E_{1^-} - E_{0^-} = -0.38\Delta + 1.38 S_\Lambda + 7.85T = 0.026 \ \ \text{MeV}[10].$$

The extracted T value is ~ 0.03 MeV.

After these experiments were sucsesfully finished, more sophisticated theoretical calculation was performed. The numerical values of the above parameters are fine tuned to be:

Δ = 0.430 MeV, S_Λ = -0.015 MeV, S_N = -0.390 MeV, T = 0.030 MeV.

One thing to be noticed is that the value of these five parameters are not constant. The numerical value usually varies depending on different hypernuclei. In the theoretical treatment, the integral to obtain the value of those parameters depends on the wave function, which, in turn, varies with different nucleus. Table 1.2 gives the values of the interaction parameters for several hypernuclei ,which were calculated by Millener based on the experimental data for ${}^{7}_{\Lambda}$Li, ${}^{9}_{\Lambda}$Be and ${}^{16}_{\Lambda}$O [16].

Table 1.2: The ΛN effective interaction parameters derived for several hypernuclei by Millener [16].

	Δ [MeV]	S_N [MeV]	S_Λ [MeV]	T [MeV]
${}^{7}_{\Lambda}$Li, ${}^{16}_{\Lambda}$O, ${}^{9}_{\Lambda}$B	0.43	−0.39	−0.015	0.030
${}^{8}_{\Lambda}$Li	0.459	−0.433	−0.011	0.027
${}^{9}_{\Lambda}$Be	0.557	−0.549	−0.013	0.029
${}^{10}_{\Lambda}$B	0.458	−0.428	−0.01	0.027
${}^{11}_{\Lambda}$B	0.488	−0.437	−0.01	0.030
${}^{12}_{\Lambda}$C	0.550	−0.50	−0.012	0.025
${}^{13}_{\Lambda}$C	0.532	−0.545	−0.013	0.027
${}^{15}_{\Lambda}$N	0.468	−0.429	−0.011	0.023

The determined parameters can reproduce many p-shell hypernuclear levels. For example, the ${}^{7}_{\Lambda}$Li$(\frac{7}{2}^+, \frac{5}{2}^+)$ spacing of 471 keV is well explained by these parameters [14]. However, as one may expect, the current phenomenological description of hypernuclear structure is still incomplete. In fact, some evidences have already appeared, for example, the inconsistency between a theoretical calculation and experiments in the case of ${}^{10}_{\Lambda}$B [15]. To essentially improve our understanding of the ΛN interaction many works are still needed. With this background, the KEK-E566 experiment was carried out at National Laboratory for High Energy Physics (KEK), Japan.

1.4 Physics Interests of the KEK-E566

In the present experiment, ^{12}C(π^+,K$^+$)$^{12}_{\Lambda}$C reaction was employed to populate $^{12}_{\Lambda}$C. Compared with the (K$^-$,π^-) in-flight reaction, the current (π^+,K$^+$) reaction is characterised by its large momentum transfer($\sim$350 MeV/c) as shown in Fig. 1.5. Thus many hypernuclear states were produced and various electromagnetic transitions can be studied in the same experiment [25]. The populated hypernuclear states can be viewed in the missing mass spec-

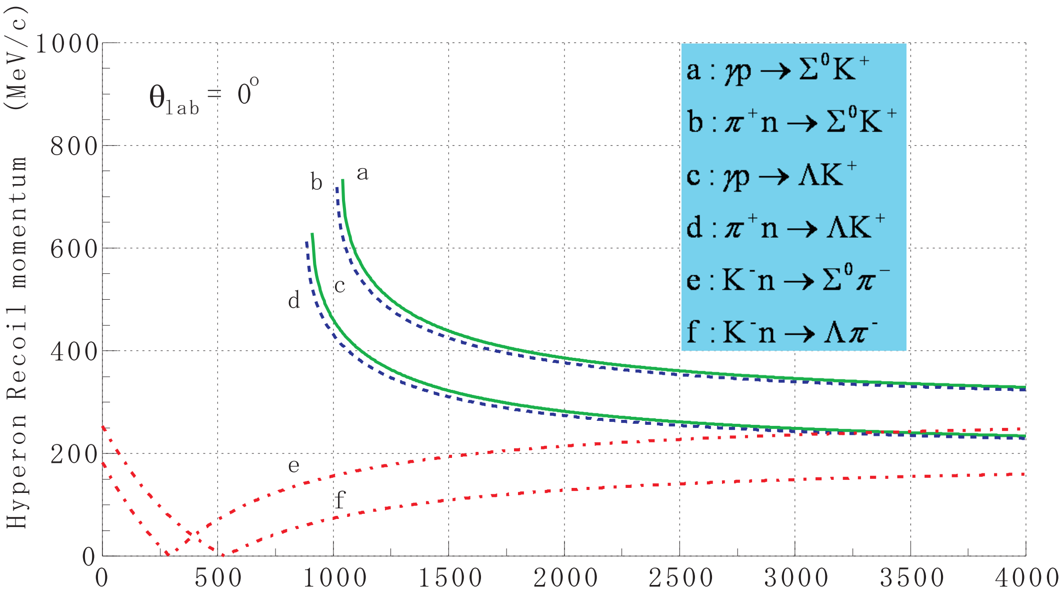

Figure 1.5: Recoil momentum of generated hyperon v.s. projectile particle momentum.

trum, which has been studied systmetically in previous reaction spectroscopy experiments at KEK [6][26]. The result for $^{12}_{\Lambda}$C is plotted in Fig. 1.6, where the level energies and cross sections calculated by Millener and Itonaga are also shown [16][17][18]. The missing mass spectrum relates the level scheme as follows: the first dominant peak(#1) from the left in the spectrum corresponds to the ground state doublets(Λ at s-orbit) in the $^{12}_{\Lambda}$C level scheme(1^-_1 and 2^-_1) where the non-spin-flip 1^-_1 state is dominantly produced over the spin-flip 2^-_1 state; the second donimant peak(#5) has contributions from many states whose main components come from the p-orbit Λ coupling to the nuclear core. The level spacing due to the spin-dependent interaction cannot be resolved in the missing mass spectrum because of the limited energy resolution. By selecting specific states in the missing mass spectrum, the hypernuclear γ rays from interested transitions can be obtained, from which the spin-dependent interactions can be studied quantitatively.

The experimental data from the present experiment are very important to test the universality of the parameters derived in the above. Besides this general value, the physics interests of the present experiment can be specified into two topics: One is to study the effects of the ΛNN three-body interaction,

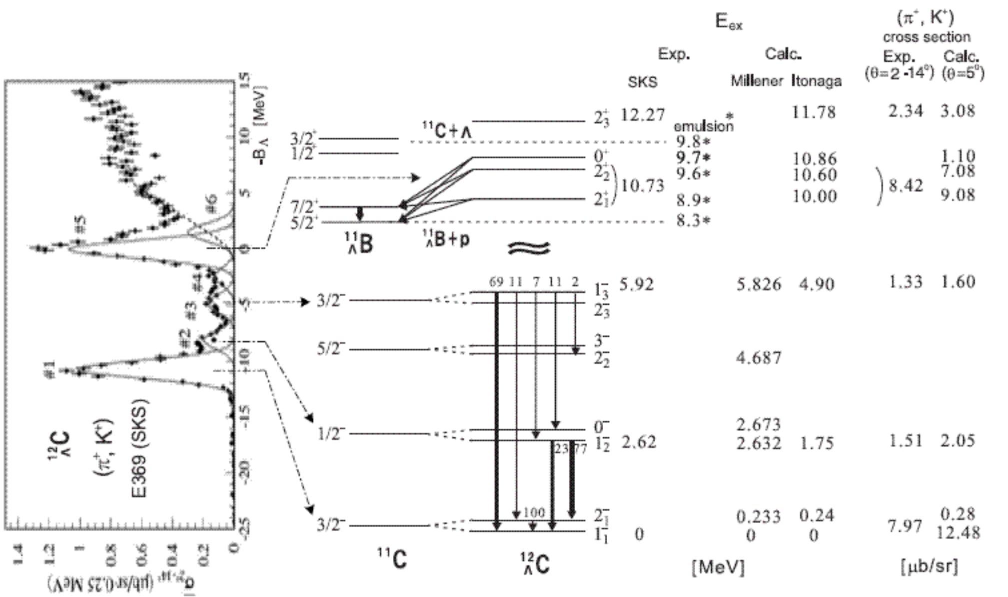

Figure 1.6: ${}^{12}_{\Lambda}$C Level Observed in KEK-E369 [6].

and another is to measure the g-factor of the Λ inside the nuclear medium. The following two subsections are devoted to the detailed discussions.

1.4.1 To Study the ΛNN three-body Interaction

In the current theoretical frame work, most of hypernuclear energy levels obtained so far are well reproduced by calculations with the experimentally derived parameters. However, as mentioned in the previous section, exceptions are also found. In the case of ${}^{10}_{\Lambda}$B , it is called ${}^{10}_{\Lambda}$B puzzle. The origin of this puzzle can be traced back to the first attempt of measuring hypernuclear γ rays with germanium detectors at BNL [19]. In this experiment, the effort to detect the γ rays emitted from the ground state doublet transition (${}^{10}_{\Lambda}$B ($2^-\to1^-$)) failed. Later, another experiment with Hyperball carried out at BNL, which accumulated more statistics, did not observe the expected γ rays either. Based on these experiments, a upper limit of the ground state doublet spacing was determined to be 100 keV. On the other hand, theory predicts

$$ {}^{10}_{\Lambda}B : E(2^-) - E(1^-) = 0.578\Delta + 1.41S_\Lambda + 0.014S_N - 1.07T = 214 \ \ \text{keV}. $$

There are several possible explanations to the disagreement, such as by modifying the wave functions or including the ΛNN three body force. The ΛNN three body force was first introduced to explain the energy levels in s-shell hypernuclei[3] [20][22].

Akaishi et al. showed that the ΛNN three body force predicted by the Nijmegen's baryon-baryon interaction models can explain all the bound states

[3]The s-shell hypernuclei has a Λ in the s-orbit and other nucleons in the s-orbit also.

The basic idea of this hyperthesis is to introduce the effect of the ΛNN three body force caused by the $\Lambda\Sigma$ coupling as shown in Fig. 1.7.

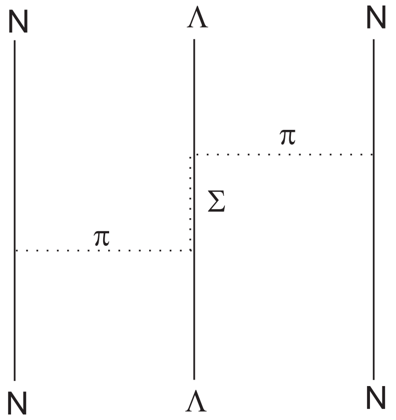

Figure 1.7: $\Lambda\Sigma$ coupling and the ΛNN three body force.

of ${}^{3}_{\Lambda}$H, ${}^{4}_{\Lambda}$H (${}^{4}_{\Lambda}$He), and ${}^{5}_{\Lambda}$He [20]. But the effect of this interaction to p-shell hypernucleus is still unknown. If we denote the energy shift due to the three body force by $\Sigma\Lambda$ and include this new term in the calculation, the ${}^{10}_{\Lambda}$B ground state doublet spacing becomes

$$ {}^{10}_{\Lambda}B : E(2^-) - E(1^-) = 214 \ \ \text{keV} + \Sigma\Lambda $$

If the $\Sigma\Lambda$ term has a negative value, then the ${}^{10}_{\Lambda}$B spacing can be smaller and the experimental data could be explained in this way. However, to verify this assumption, we need a hypernuclear system in which the three body effects can be clearly observed. The theory shows that the $\Sigma\Lambda$ term has opposite effects on ${}^{10}_{\Lambda}$B from ${}^{12}_{\Lambda}$C . Thus we should expect the ground state doublet of ${}^{12}_{\Lambda}$C to have a energy spacing larger than the value

$$ {}^{12}_{\Lambda}C : E(2^-) - E(1^-) = 0.474\Delta + 1.51S_\Lambda + 0.031S_N - 2.092T = 167 \ \ \text{keV}, $$

which is predicted barely from the original effective interaction parameters. In another word, the energy spacing of ${}^{12}_{\Lambda}$C ground state should provide a direct test for this three body interactions effect to the p-shell hypernucleus.

1.4.2 To Measure the g-factor of Λ Hyperon inside Nuclear Medium

The magnetic momentum of a Λ hyperon has long been known to be

$$ g_\Lambda = -1.226 \pm 0.008[\mu_N]. $$

But the g_Λ in the nuclear media may be different from this value. The measurement of g_Λ is interesting because it can tell us the baryon medium effects and shed light on the understanding of the partial restoration of the chiral symmetry. The g_Λ is related to the Λ-spin-flip transition probability in a time-dependent perturbation treatment. Measurement of $B(M_1)$ leads to determination of g_Λ via the following expression,

$$\begin{aligned}
B(M1) &= (2J_{up}+1)^{-1}| < \phi_{low}|\mu|\phi_{up} > |^2 \\
&= (2J_{up}+1)^{-1}| < \phi_{low}|g_{core}J_{core} + g_\Lambda J_\Lambda|\phi_{up} > |^2 \\
&= (2J_{up}+1)^{-1}| < \phi_{low}|g_{core}J + (g_\Lambda - g_{core})J_\Lambda|\phi_{up} > |^2 \\
&= \frac{3}{8\pi}(2J_{low}+1)(2J_{core}+1)^{-1}(g_{core}-g_\Lambda)^2 \quad [\mu_N^2],
\end{aligned}$$

where the ϕ_{low} and ϕ_{up} stand for the wave functions of the ground state (spin-non-flip) and excited state (spin-flip), respectively. J_{core} and J_Λ are the total angular momentum operator of the nuclear core and the Λ particle. g_{core} and g_Λ are the g-factors for the Λ and nuclear core, respectively. If branching ratio for the excited state going to the ground state is 100 %, B($M1$) can also be related with the lifetime τ as

$$\frac{1}{\tau} = 1.76 \times 10^{13} \cdot B(M1) \cdot E_\gamma^3 \quad [\mathrm{s}^{-1}],$$

where the E_γ is the γ-ray energy corresponding to the Λ-spin-flip transition. To obtain g_Λ, we only need to know τ and E_γ. E_γ can be measured with Hyperball2, while τ may be obtained from the Doppler Shift Attenuation Method (DSAM), which will be introduced in Chaper 3. In the present experiment, there is an ideal transition that can be unitilized ${}^{11}_{\Lambda}\mathrm{B}(7/2^+ \rightarrow 5/2^+)$, which is produced via the proton emission from the p_Λ states of ${}^{12}_{\Lambda}\mathrm{C}(2^+)$. Another merit of current experiment is that there are no other γ-ray transitions are mixed when gating the fifth peak in the Fig. 1.6 as a result of a previous Hyperball experiment (KEK-E518) [21].

Chapter 2

Experimental Setup

2.1 Outline

Our experiment was performed at National Laboratory for High Energy Physics (KEK), Japan, with its secondary beam line (K6) from the 12 GeV Proton Synchrotron (PS).

In the present experiment, the central momentum of π^+ beam was set at 1.05 GeV/c because the $\pi^+ n \rightarrow \Lambda K^+$ reaction has a sharp maximum at this beam energy for scattered angle at 0^o as shown in Fig. 2.1. The outgoing K^+ mesons have a momentum around 0.75 GeV/c.

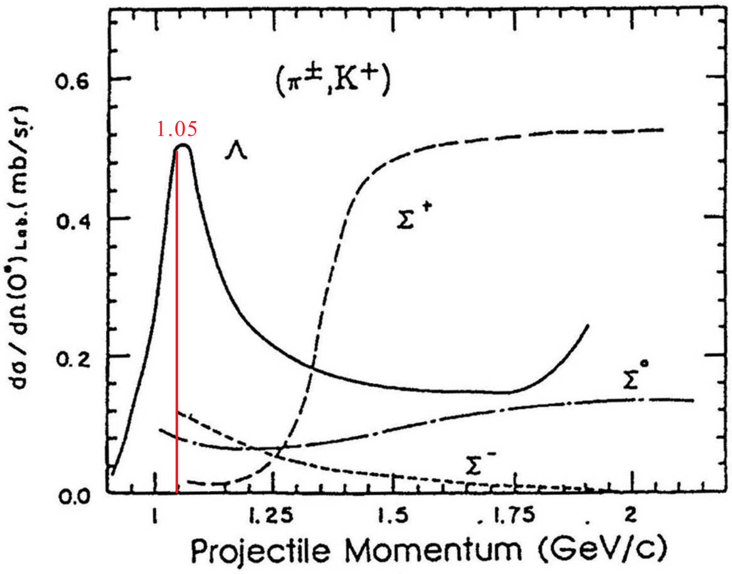

Figure 2.1: Cross section of the elementary process π N $\rightarrow \Lambda$ K as a function of the projectile momentum.

The experimental setup of the present experiment mainly consists of three parts: the incident particle spectrometer (beam line spectrometer, including the beam line), the scattered particle spectrometer (the SKS spectrometer) and the γ-ray detection system (Hyperball2[1]). They will be discussed in this order. The whole schematic view of the experimental setup is shown in Fig. 2.2

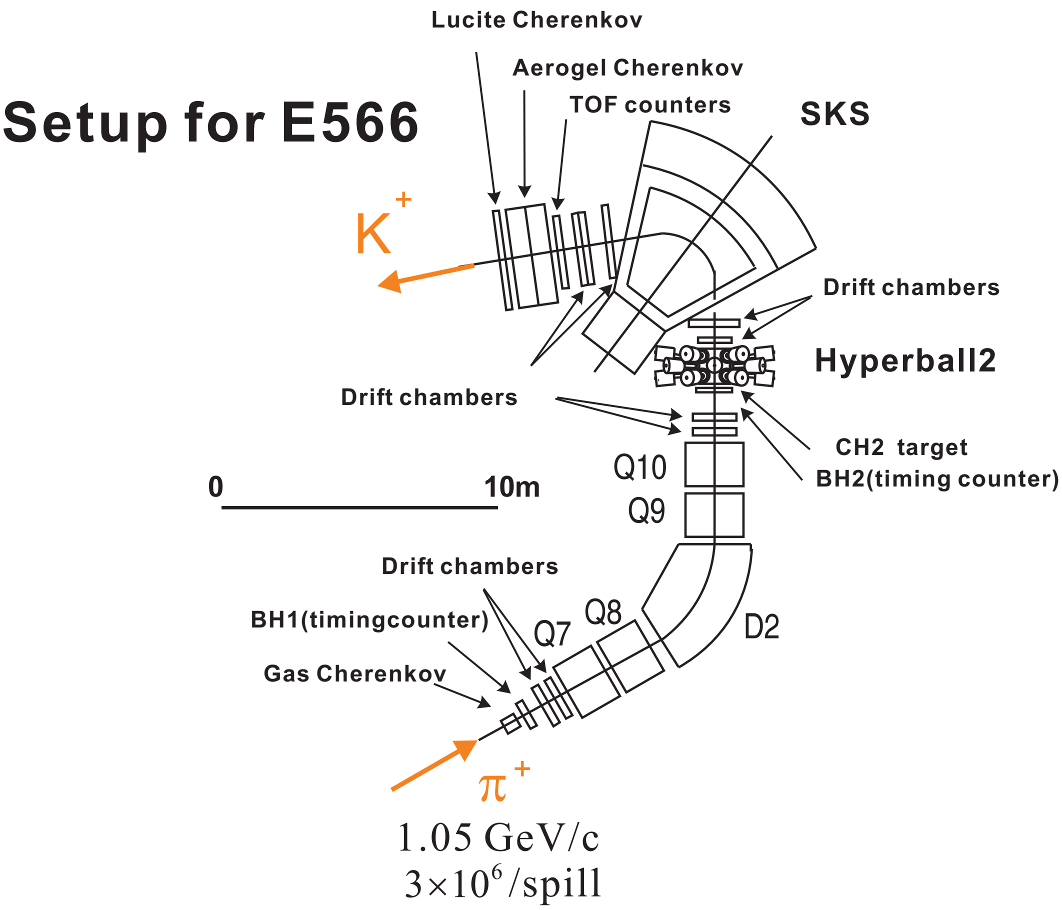

Figure 2.2: Schematic view of experimental setup.

[1]An upgraded version of the original Hyperball. For details of the original Hyperball, see [15].

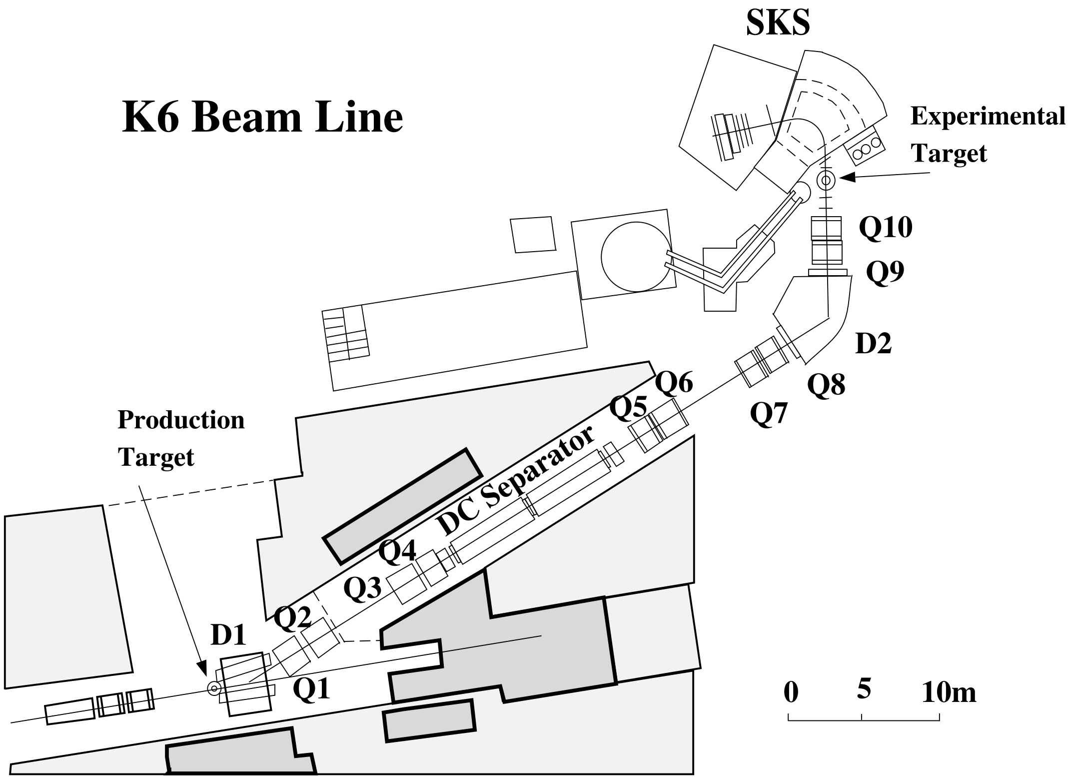

Figure 2.3: KEK-PS K6 beam line.

2.2 Beam Line and Beam Line Spectrometer

. ***K6 beam line***

The K6 beam line is a general-purpose high-intensity beam line that can supply various mass-separated secondary beams in the momentum range from 0.5GeV/c to 1.4 GeV/c [27]. Fig. 2.3 shows a schematic view of the K6 beam line. The beam line consists of two dipole magnets (D1, D2), ten quadruple magnets (Q1-Q10), a sextuple magnet (SX), an electrostatic separator (DC separator) with two correction magnets (CM1, CM2) and four slits. The slits are installed between D1 and Q1 (acceptance slit), between Q2 and Q3 (intermediate focus slit), between SX and Q5 (momentum slit) and between Q6 and Q7 (mass slit). The primary proton beam was extracted for a period of 1.5 sec. in every cycle of 4.0 sec. synchronized to the KEK 12-GeV PS operation cycle. The secondary pions were produced by the primary proton beam impinging on a production target located at the most upstream of the K6 beam line. The intensity of primary protons on the production target (60 mm thick platinum) was typically 1×10^{12}/spill. The main components of the K6 beam line are summarised as Table 2.1.

Table 2.1: The specification of the K6 beam line

Name	Comment
SEC	Secondary Emission Chamber
Production Target	60 mm thick platinum
TM	Target Monitor
Acceptance Slit Vertical	Brass 8cm thick
Acceptance Slit Horizontal	Brass 12cm thick
Q1	
Q2	
IF Slit Vertical	Brass 1m; Intermediate Focus Position
Q3	
Q4	
CM1	Correction Magnet
ES	ES Separator, top(Negative) & Bottom(Positive)
CM2	Correction Magnet
SX	Sextupole Magnet
Momentum Slit Horizontal	Brass 15cm thick
Q5	
Q6	
Mass Slit Horizontal	Brass 1m thick
Q7	QQDQQ system
Q8	QQDQQ system
D2	QQDQQ system
Q9	QQDQQ system
Q10	QQDQQ system

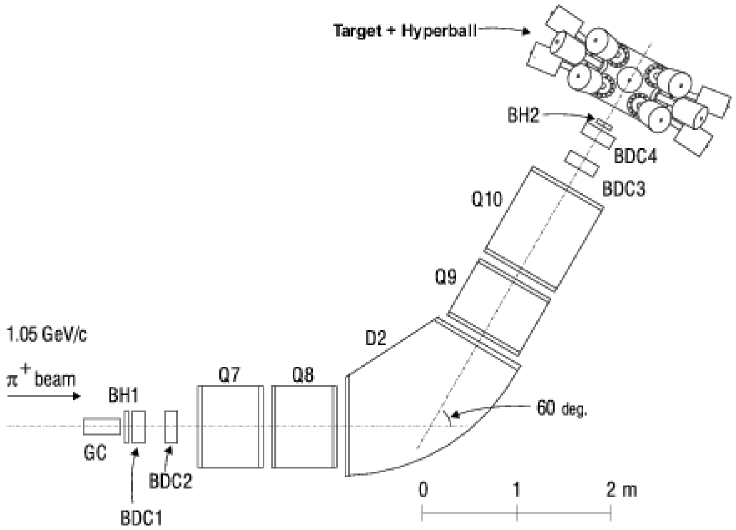

Figure 2.4: Schematic view of the spectrometer for the incident pion.

Beam line spectrometer

The momentum distribution of the produced π^+ beam is rather broad due to the quality of the secondary beam. To achieve a good energy resolution, the momentum of π^+ particles was measured event by event with the end part of the K6 beam line which works as a spectrometer. As shown in Fig. 2.4, the beam line spectrometer consists of a QQDQQ magnet system with four sets of drift chambers (BDC1,2,3,4) and three sets of trigger counters. The trigger counters include a Freon-gas Čerenkov counter (eGC) and two sets of segmented scintillation counters (BH1,BH2). The beam spectrometer has a momentum resolution of 0.1 % (FWHM) at 1 GeV/c [26]. A third-order transfer matrix was used for the momentum reconstruction. To reduce the scattering during the transportation, the beam pipe in the QQDQQ system was kept as vacuum with a Kapton window of 100 μm thickness, and the tracking chambers were also made as thin as possible. The magnetic field of the D2 magnet was monitored during the experiment with a high-precision Hall probe in order to correct its fluctuation in the off-line analysis. The observed fluctuation was within ± 0.01 %. Design specifications of the beam line spectrometer are listed in Table 2.2.

Table 2.2: The specification of the beam line spectrometer.

Momentum resolution	0.1 % (FWHM) at 1 GeV/c
Momentum bite	± 3 %
Maximum central momentum	1.2 GeV/c
Bending angle	60°

2.2.1 Trigger Counters

The main contamination in the π^+ beam after the DC separator and the mass slits are the positrons and protons, of which fractions are $\sim$20 % and $\sim$10 %, respectively, while the K^+ contamination is negligible because most of the K^+ that have the same momentum have decayed before reaching the target [6]. These background particles were rejected by the trigger counters effectively. The eGC has an index of 1.00245 which is only sensitive to positrons and has the efficiency of more than 99%. The protons that passed the QQDQQ system were vetoed by the time of flight information provided by BH1 and BH2. The schematic views of BH1 and BH2 are shown in Fig. 2.5 and Fig. 2.6.

The BH1 and BH2 were designed to stand for a high counting rate and to minimise the π^+ scattering in these two scintillators. The BH2 is 6 mm thick. The size of each segment is varied to make the counting rate of each segment equal. In addition, BH2 also serves as the time origin of the whole system.

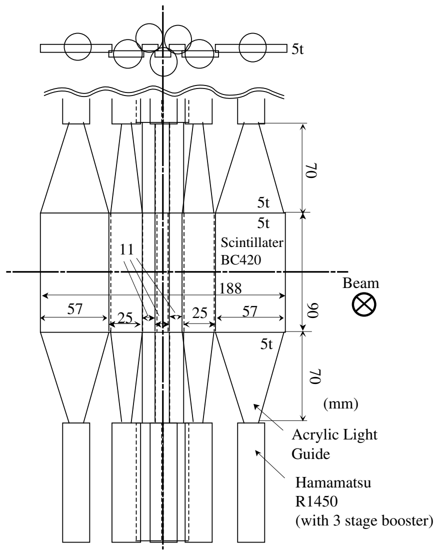

Figure 2.5: Schematic view of BH1.

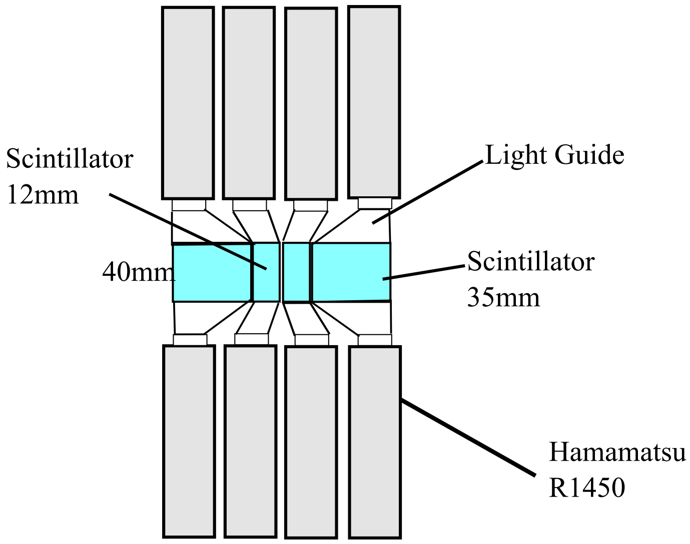

Figure 2.6: Schematic view of BH2.

2.2.2 Drift Chambers

Four sets of drift chambers (BDC1,2,3,4) were used for the beam particle track reconstruction. The details of the track reconstruction and the procedure of momentum determination will be described in Chapter 3. BDC1 and BDC2 were located at the entrance of QQDQQ system while BDC3 and BDC4 were placed at the exit of QQDQQ and before the target. The structure of the beam drift chambers is shown in Fig. 2.7 and Fig. 2.8. In each plane, 48 sense wires were separated from each other by potential wires with 2.5 mm distance. The sense wires were gold-plated tungsten wires of 12 μm-diameter. The material used for the 75 μm-diameter potential wires was copper-beryllium. Each BDC consists of three sets of pair planes whose tilt angles are +15°(u, u'), 0°(x, x'), -15°(v, v'), respectively, if we choose the vertical direction as zero degree. This configuration can optimise the horizontal spacial resolution which is more important than the vertical direction in the track reconstruction. To solve the left-right ambiguity, the pair plane method[2] was used.

To minimise the effect of multiple scattering and to stand for a high counting rate, the BDCs were made as thin as possible: the spacing between two pair planes is about 5 mm. The chamber gas was a mixture of Ar(76%)+C_4H_{10}(20%)+Methylal(4%). The detection efficiency was typically 99%.

[2]Two planes that have identical structure were shifted by 2.5 mm from each other as shown in Fig. 2.8.

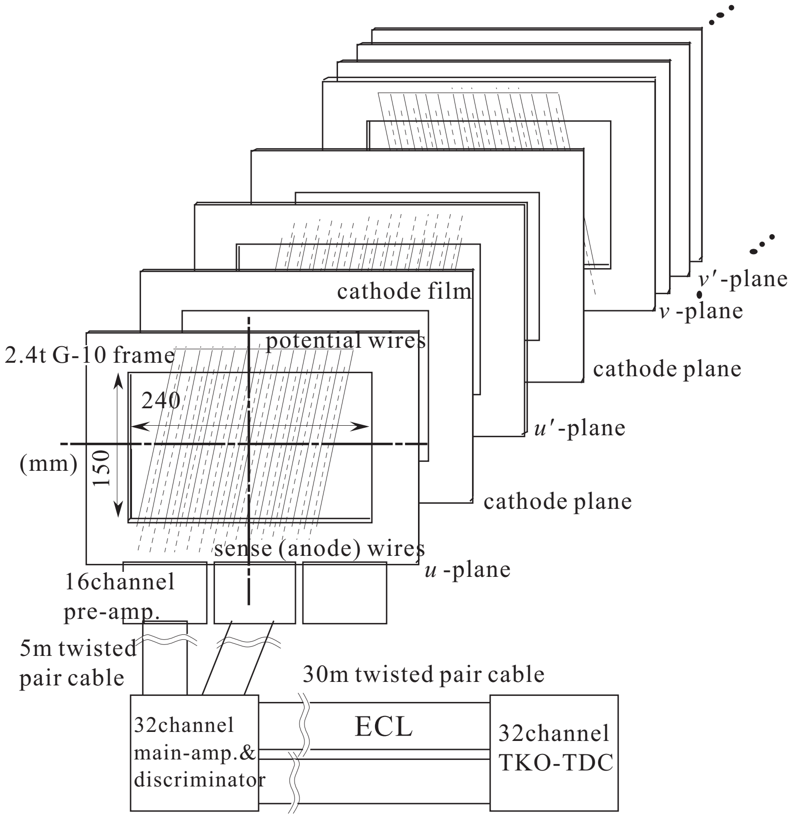

Figure 2.7: Schematic view of BDC and read-out system.

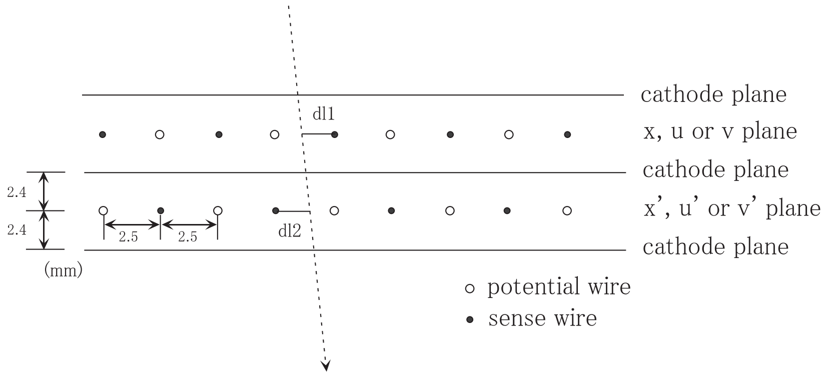

Figure 2.8: BDC cell structure of the pair plane.

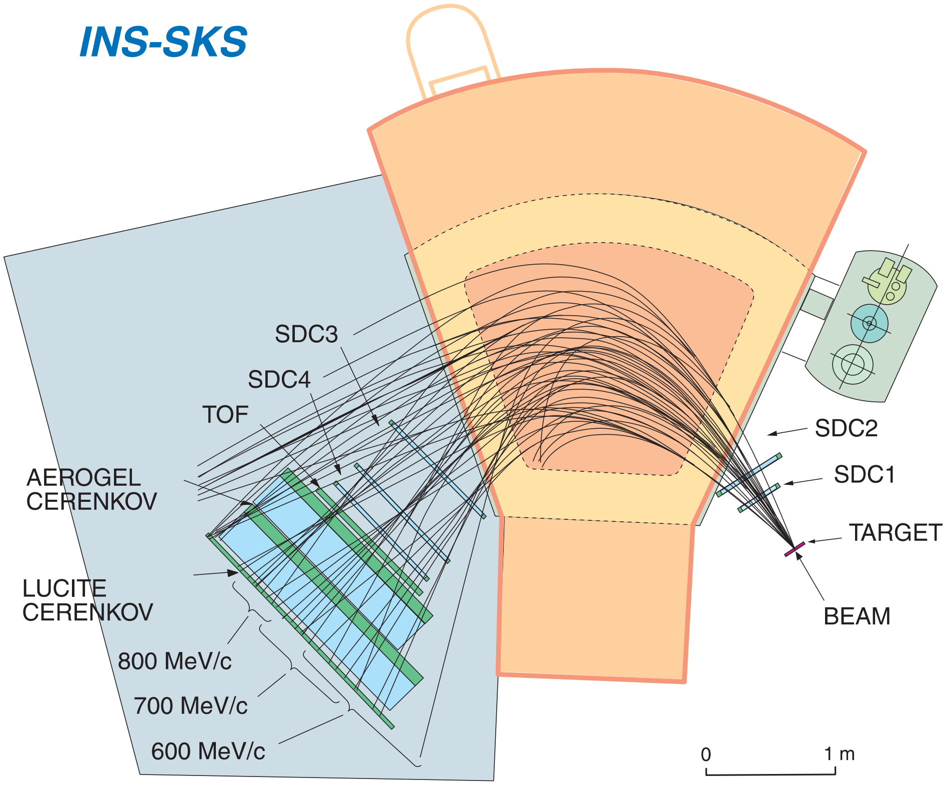

Figure 2.9: Schematic view of SKS.

2.3 Scattered Particle Spectrometer — SKS Spectrometer

SKS (Superconducting Kaon Spectrometer) spectrometer consists of four sets of drift chambers (SDC1,2,3,4), a superconducting dipole magnet (SKS magnet) and three types of trigger counters (Tof, AC1,2 and LC). The remarkable feature in the current system is its outstanding momentum resolution. Combined with the beam line spectrometer, the SKS spectrometer provides the best energy resolution, ~1.4 MeV (FWHM), achieved in the hypernuclear spectroscopy study for a long time till recently [6][29]. Design criteria of SKS are: a large acceptance(100 msr), a good momentum resolution(0.1% at 0.72GeV/c) and a short path length(5 m) to minimise the kaon in-flight decay. The magnetic field of SKS was set at 2.2 T (272 A) in order to make 0.72 GeV/c particles pass along the central orbit. The detailed parameters for SKS is listed in Table 2.3. Fig. 2.9 shows the schematic view of SKS.

2.3.1 Trigger Counters

Three types of trigger counters worked in conjunction with the drift chambers and SKS. They were Tof, AC1,2 and LC. The Tof was a set of plastic

Table 2.3: The specification of SKS.

Momentum resolution	0.1 % (FWHM) at 0.72 GeV/c
Momentum bite	$\pm$10 %
Maximum central momentum	1.1 GeV/c
Bending angle	100° for the central trajectory
Solid angle	100 msr
Flight path	$\sim$ 5 m for the central trajectory

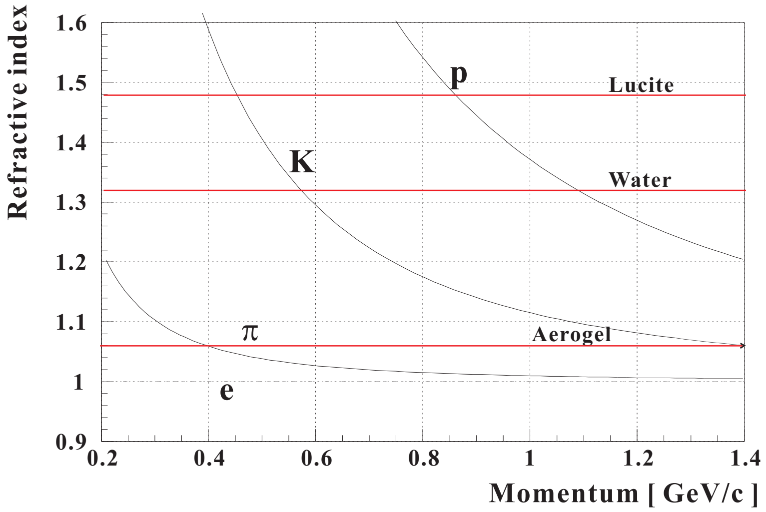

Figure 2.10: Index and threshold v.s. momentum curve.(Water is past for reference.)

scintillation counters. AC1,2 and LC were Čerenkov counters.

AC1,2 (silica aerogel Čerenkov counters) and LC (Lucite Čerenkov counter) rejected π^+ and protons in the trigger level. The index of AC1,2 is 1.06 and it can veto pions with a momentum higher than 0.4 GeV/c. The index of LC is 1.495 and it can veto protons with a momentum higher than 0.85 GeV/c by anti-coincidence. The indexes of aerogel and lucite together with the threshold momentum as a function of momentum are shown in Fig. 2.10.

The Tof was made of 15 pieces of plastic scintillators and served as a time-of-flight detector for particle identification. The typical time resolution between BH2 and Tof is about 200 ps in rms where the flight path between them is about 4.5 m. The schematic drawing of the Tof is shown in Fig. 2.11.

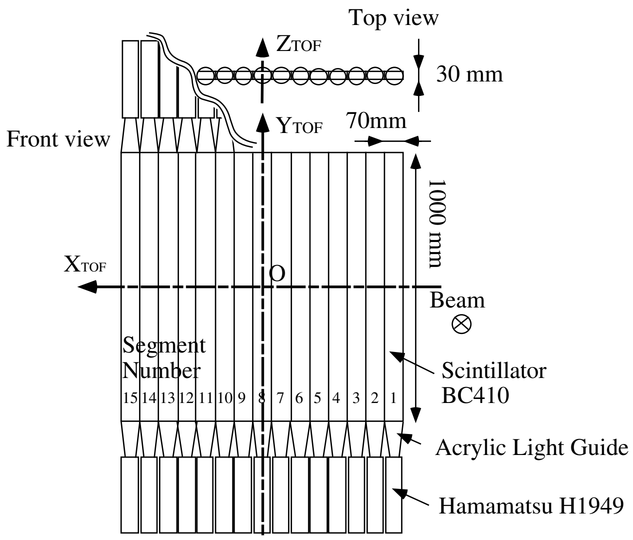

Figure 2.11: Schematic view of Tof.

The AC1 and AC2 were essentially the same except their size. The sensitive area of AC1 was $105 \times 120 \times 9$ cm^3 and that of AC2 was $140 \times 140 \times 12$ cm^3. The schematic view of AC1 is shown in Fig. 2.12.

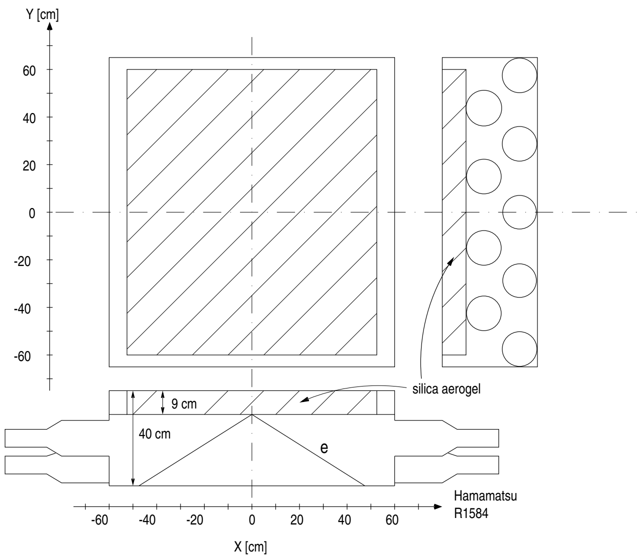

Figure 2.12: Schematic view of AC1.

The LC had 14 segments of $10\times140\times4$ cm^3 lucite radiators. The schematic view of LC is shown in Fig. 2.13

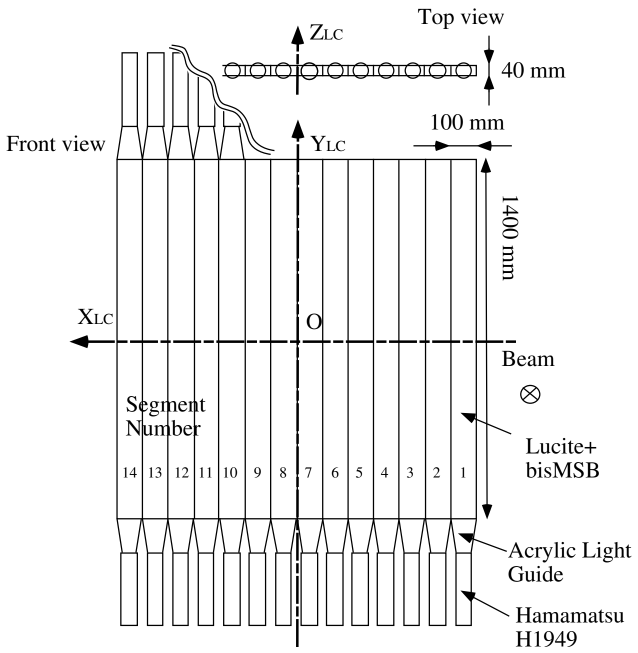

Figure 2.13: Schematic view of LC.

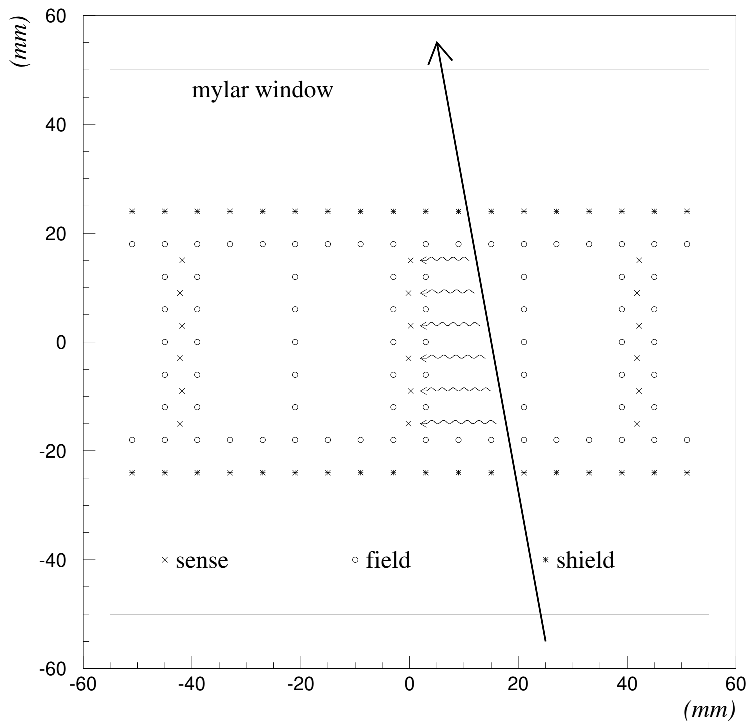

Figure 2.14: Wire configuration of SDC4.

2.3.2 Drift Chambers

Four sets of drift chambers, SDC1, SDC2, SDC3 and SDC4, served to reconstruct the track of scattered particles. SDC1 had the same plane structure as BDC but only two sets of pair planes (uu', vv') were included instead of three. SDC2 also had the same cell structure as BDCs but with a larger size (80 wires instead of 48) to detect scattered particles effectively. SDC3 and SDC4 had different structures, particularly, a larger drift space which is possible due to the lower counting rate of the scattered particles that can pass the SKS magnet. SDC3 consisted of x, x' and y, y' plane with a drift length of 21 mm. SDC4 was separated into two chambers: SDC4X and SDC4Y. Each of these chambers had six planes with different relative positions, as shown in Fig. 2.14. The chamber gas was a mixture of Ar(50%)+C_4H_{10}(50%).

The design parameters of SDC are summarised in Table 2.4.

Table 2.4: Specification of the drift chambers.

Name	Effective area (cm^2)	Maximum drift length (mm)	Planes	Resolution (μm in rms)
BDC1,2,3,4	$24^W \times 15^H$	2.5	$xx'uu'vv'$	300
SDC1	$24^W \times 15^H$	2.5	$uu'vv'$	300
SDC2	$40^W \times 15^H$	2.5	$xx'uu'vv'$	300
SDC3	$100^W \times 100^H$	21	$xx'yy'$	250
SDC4	$100^W \times 100^H$	21	$x \times 6, y \times 6$	250

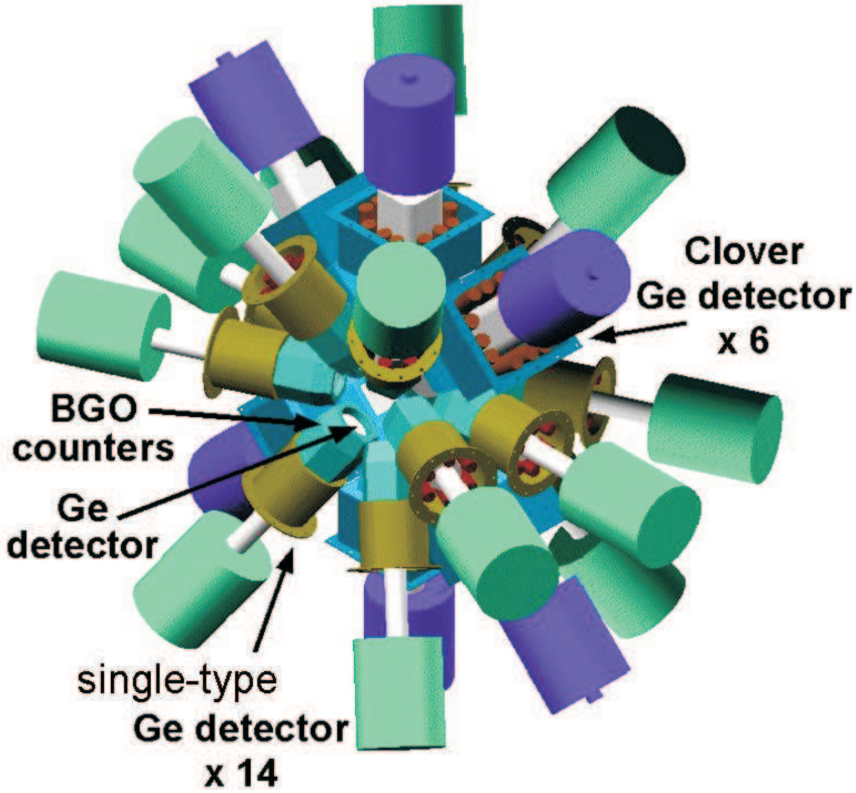

Figure 2.15: Schematic view of Hyperball2.

2.4 γ-ray Detecting System — Hyperball2

To detect γ rays emitted from the populated hypernucleus, we used a germanium detector array called Hyperball2. In order to increase the detection efficiency, we upgraded the previous array, Haperball, into Hyperball2 by increasing the total Ge detector volume nearly twice. The schematic view of Hyperball2 is shown in Fig. 2.15. Hyperball2 has total of 14 single crystal type germanium detectors (single Ge) and 6 clover-type germanium detectors (clover Ge), each of them was surrounded by the bismuth germanate (BGO) counters to suppress the background signal that mainly caused by

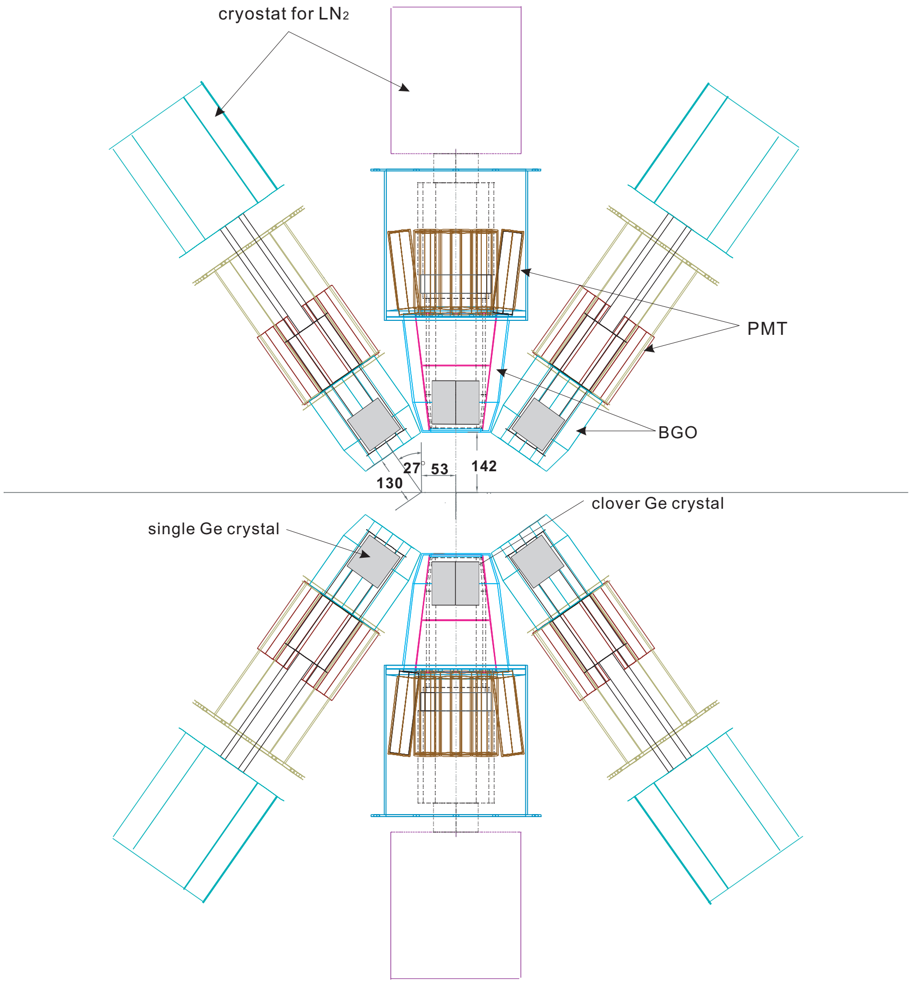

Figure 2.16: Cross sectional view of Hyperball2.

Compton scattering. A ^{60}Co pulser[3] was also equipped on every Ge detector to monitor the efficiency and energy resolution during the beam time. The configuration of Hyperball2 is shown in Fig. 2.16. Six out of fourteen single detectors were located in the upstream ring (90 degree - 27 degree), four clover type plus two single detectors were installed in the middle ring (90 degree) and the other six single detectors were placed in the down stream ring. The distance from the surface of the germanium detectors to the target center is about 15 cm. In order to increase the suppression efficiency, the BGO counters were located 2 cm closer to the target. This can also be seen from Fig. 2.17. Hyperball2 covers 25% of total 4π solid angle. The total peak efficiency is about 5% for 1 MeV γ ray.

[3] A ^{60}Co source assembled with plastic scintillators and a photo-tube. The detailed description will be given in the following section.

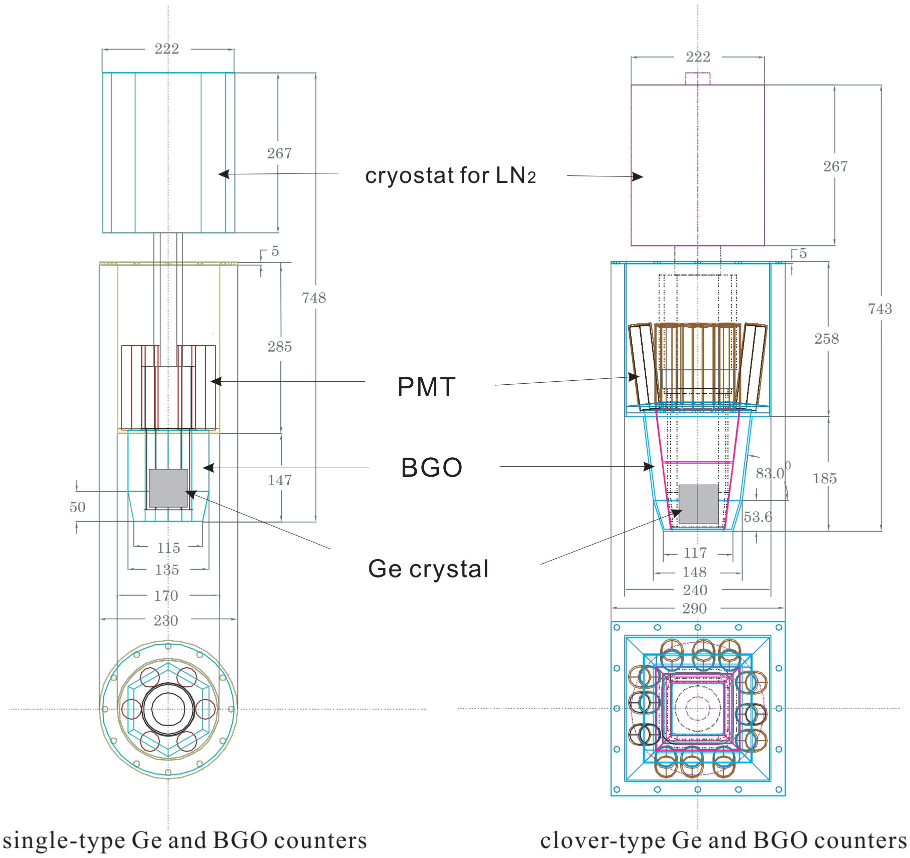

Figure 2.17: Cross sectional view of the assembled detectors.

2.4.1 Germanium Detectors

The single Ge had a ~250 cm^3 (70 mmϕ×70 mm) high-purity cylindrical germanium crystal. The clover Ge consisted of four segments of (45 mm× 45 mm× 71 mm) high-purity germanium crystals. The relative efficiency[4] is about 60% for the single Ge and 20% for each segment in the clover Ge. In the clover Ge detector, the efficiency goes up to 120% when including the add-back events.[5] The Ge detectors in Hyperball2 were made of n-type semiconductors, which are more endurable to radiation damage [30]. The detectors were equipped with so called reset-type preamplifiers, whose schematic circuit and the typical signal shape from the preamplifier are shown in Fig. 2.18. This technique was also known as active reset preamplifier [30]. The maximum deposited energy allowed by the preamplifier before its reset is about 150 MeV. (The energy given by the high energy mesons when they penetrate the Ge detectors was around 50 MeV.) It was found that the reset rate is about 3 kHz in the present experiment. The dead time caused by discharging the circuit is about 10 ~ 20 μsec, and consequently the dead time is about 3~6%.

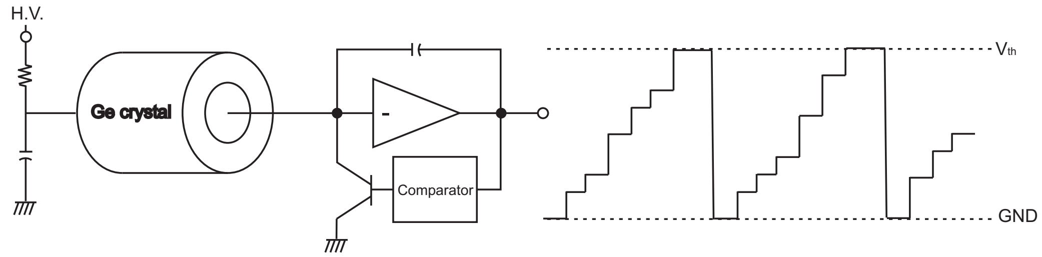

Figure 2.18: Circuit of the transistor reset-type preamplifier.

The other read out electronics were also organised to have a good performance under high counting rate. The main amplifier was a so called Ultra High Rate Amplifier (ORTEC 973). In this module, a gated integrator, whose integration time was 3 μsec, was connected after a fast shaping amplifier to correct the deformed signal shape. The output from main amplifier was sent to the Amplitude Digital Converter (ORTEC AD413A) to prepare for the data acquisition system (DAQ). The Ge detector signal was also processed by Time Filter Amplifier (TFA: ORTEC 579 Fast-Filter Amp.) and Constant Fraction Discriminator (CFD) successively to obtain timing information. The timing signal from the output of CFD was sent to miltihit TDC (LeCroy 3377). The circuit for one detector is illustrated in Fig. 2.19.

[4]We use a 3"ϕ×3" NaI(Tl), as 100% efficiency for 1.33 MeV γ ray, to calibrate our germanium detectors.

[5]If one γ ray hits more than one segment inside the clover Ge, all the energy deposited in these segments can be added up to reconstruct the full energy peak. By this means, the total efficency of clover Ge is increased.

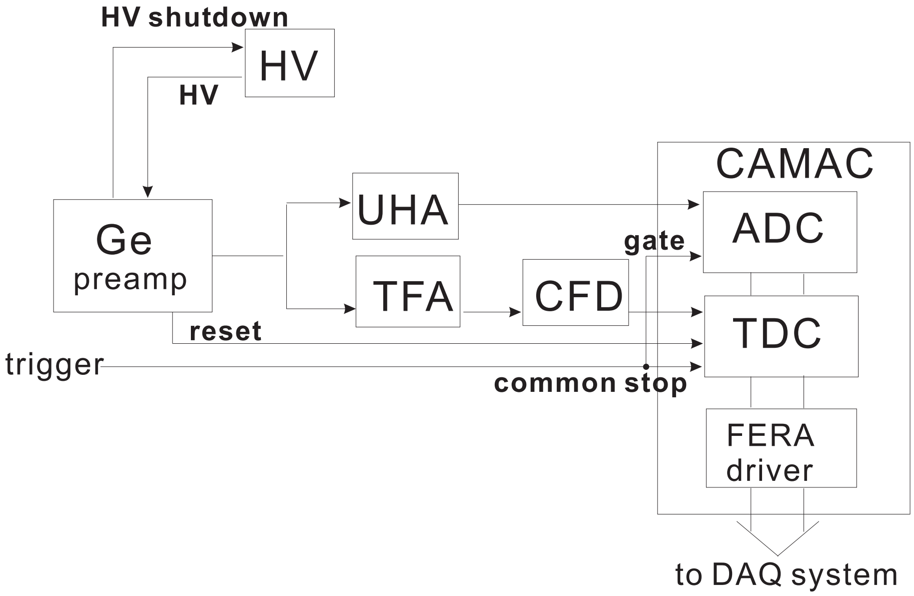

Figure 2.19: Circuit diagram for one unit of Ge detector.

2.4.2 BGO Counters

Each Ge crystal was surrounded by the BGO scintillation counters to veto the background caused by Compton scattering as well as high energy back ground γ rays and charged particles. Two types of the BGO configurations were prepared to suit the single and clover Ge detector type. The schematic view of the BGO crystal and the assembled unit were drawn in Fig. 2.20 and Fig. 2.21.

One photomultiplier tube (PMT) was attached at the end of each BGO crystal. The surface of the BGO crystal was covered with Teflon tape to increase the number of photons that can enter the PMT. Because the decay constant of BGO is about 300 ns and the light yield is relatively low, the threshold of BGO discriminator was set to accept the signal from a single photon. For example, the output from the phototube for the single photon signal has an amplitude around 20$\sim$ 30 mV. Consequently, the threshold of the discriminators for BGO was set at 10 mV to achieve a good suppression efficiency. The time resolution of BGO was about 3$\sim$ 5 nsec (FWHM) at 1 MeV.

2.4.3 ^{60}Co Pulser

The ^{60}Co pulser contained a ^{60}Co source which was embedded into a case together with a plastic scintillator and was connected to a PMT to detect photons from the scintillator. The coincidence of a PMT signal from a ^{60}Co β ray and a Ge detector signal was used as the trigger to record γ rays from ^{60}Co. The data acquired with this trigger can be employed to monitor the performance, such as energy resolution and efficiency, of Ge detector during one month beam time.

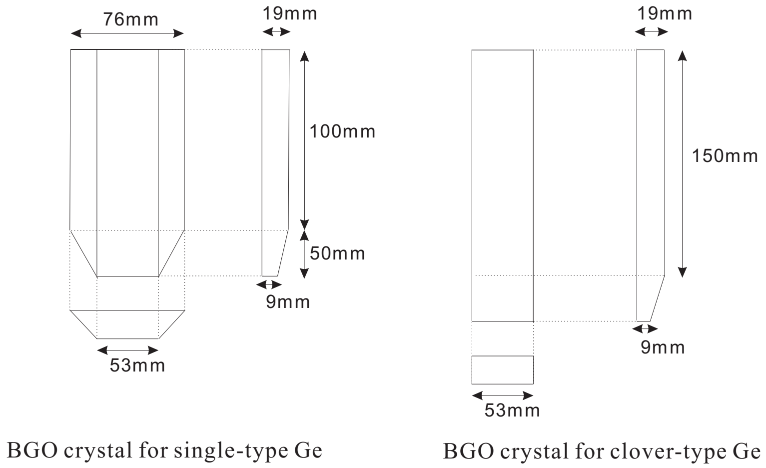

Figure 2.20: BGO Crystal.

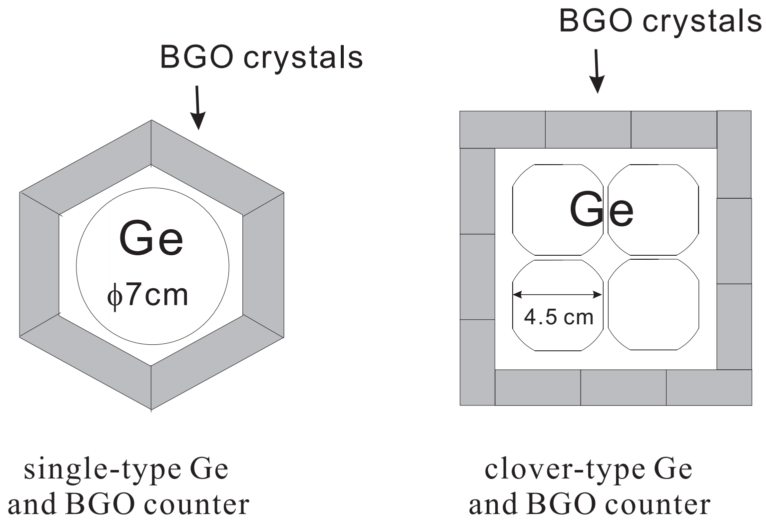

Figure 2.21: Configuration of Germanium and BGO.

2.5 Target

Our experimental target nucleus was ^{12}C. Two different targets that contained ^{12}C were used. One was a 2 cm thick carbon (graphite) target, which was used as a reference target to confirm the analysis result and the experimental condition of the present experiment for consistency with previous data using SKS. The result will be described in Chapter 3. The main experimental target material was polyethylene $(CH_2)_n$ with a density of 0.93 g/cm^3 and a volume of 50 mm$\phi\times$200 mm. Both of them are shown in Fig. 2.22.

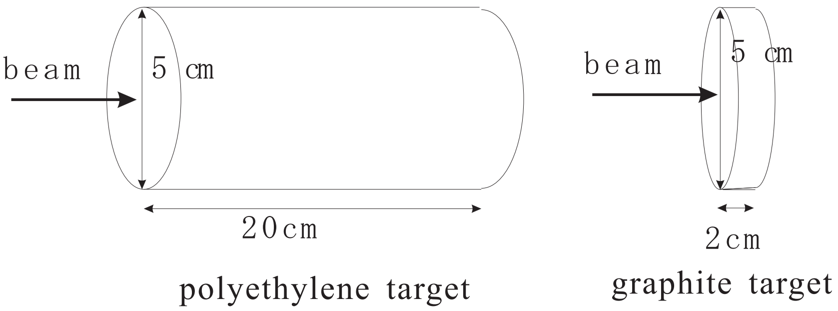

Figure 2.22: Targets used in KEK-E566. Left: $(CH_2)_n$ experimental target; right: reference target.

2.6 Trigger, Data Acquisition System and Data Summary

Trigger used in the KEK-E566 experiment

Several types of triggers were used in the present experiment for various purposes. The π^+ beam trigger was defined as:

$$BEAM = \overline{eGC} \times BH1 \times BH2.$$

The anti-coincidence of eGC was required to veto the positron contaminations. The timing information of BH1 and BH2 provided the beam time-of-flight, which was used to reject protons. The outgoing K$^+$ was defined as:

$$\mathrm{K}^+ = Tof \times LC \times \overline{AC1} \times \overline{AC2},$$

and the outgoing π^+ was defined as:

$$\pi^+ = Tof \times LC \times AC1 \times AC2.$$

The combination of the π^+ beam and outgoing K$^+$ triggers was used as the π^+K$^+$ trigger to accept the candidates of the $^{12}\mathrm{C}(\pi^+,K^+)\,^{12}_{\Lambda}\mathrm{C}$ reaction:

$$\pi^+\mathrm{K}^+ = \mathrm{BEAM} \times \mathrm{K}^+.$$

If the outgoing particle is π^+, the $\pi^+\pi^+$ trigger was made:

$$\pi^+\pi^+ = \mathrm{BEAM} \times \pi^+,$$

which can be used as an efficiency monitor for the chambers. The ^{60}Co pulser signal worked as another trigger. During both beam on and off periods, the ^{60}Co trigger was used to check the performance of Ge. But the ^{60}Co trigger was prescaled to avoid the competition with the π^+K trigger.

Data acquisition system

The TDC and ADC used for detectors other than Hyperball2 in the present experiment were manufactured under the TKO standard [28]. The signals from these modules were sent to six sets of Symmetric Memory Partner (SMP). The data acquisited during one spill were stored in SMP and were transported to a computer when beam was off. The TDC and ADC signals from Hyperball2 were sent to a Universal Memory Module (UMEM) via FERA bus during spill on. The data stored in UMEM were sent to the computer when beam was off. All the data sent to the computer were recored with a DVD-RAM.

Data summary

At the beginning of the present experiment, data of a few beam-through (without target) runs were acquired. The SKS magnet was turned off during one of these beam-through runs to check the drift chambers position. Other beam-through runs were performed with the beam momentum at 0.72 GeV/c in order to calibrate the SKS magnetic field. The data acquired in the present experiment are summarised in Table 2.6.

Table 2.5: Data summary.

Target	Number of iradiated π^+	Beam Momentum
CH_2	2×10^{12}	1.05 GeV/c
^{12}C	6×10^{9}	1.05 GeV/c
Empty	8×10^{4}	0.72 GeV/c

Chapter 3

Data Analysis

3.1 Outline

The analysis process consists of two major steps:

Mass spectrum analysis

The main task for the mass spectrum analysis is to calculate the kinematic variables and reconstruct the tracks of the particles. Then the mass of the populated hypernucleus can be calculated as

$$M_{HY} = \sqrt{(E_\pi + M_A - E_K)^2 - ({p_\pi}^2 + {p_K}^2 - 2p_\pi p_K \cos\theta_{\pi K})}, \tag{3.1}$$

where the M_{HY} is the total mass of the hypernucleus, M_A is the mass of the target nucleus, E_π (E_K) and p_π (p_K) are the energy and momentum of the incident π^+ (scattered K^+), respectively. $\theta_{\pi K}$ is the angle between π^+ and K^+. The binding energy of the Λ can be derived as

$$B_\Lambda = M_{A-1} + M_\Lambda - M_{HY}, \tag{3.2}$$

in which B_Λ is the binding energy of the Λ , M_{A-1} stands for the mass of the nuclear core and M_Λ is the mass of the Λ . The events in which interested hypernuclear states were populated can be selected by gating the M_{HY} (or B_Λ) spectrum. The γ rays emitted from the selected events were analysed further in the next step.

γ ***ray spectrum analysis***

The γ rays emitted from the interested hypernucleus need to be analysed in detail. The accidental γ rays were removed from the γ-ray energy spectrum by cutting γ-ray timing information based on ADC-TDC correlation at beginning. Then the energy calibration of the Ge detectors was performed. Background suppression using BGO TDC information was also optimised. The Doppler shift correction was applied if necessary.

3.2 Mass Spectrum Analysis

In the mass spectrum analysis, the (π^+, K^+) event was selected first with the counters and the chambers. The kinematic variables of the candidate events were calculated in two parts; the incident π^+ was analysed by the beam line spectrometer then the track of the scattered K^+ was reconstructed by the SKS spectrometer. The reaction vertex point and the missing mass of the populated hypernucleus were calculated with the kinematic variables obtained above.

3.2.1 Event Selection

The background particles can make triggers in the hardware level. Some unwanted physical process such as the (π^+, p) event can also be recorded as a (π^+, K^+) event[1] with certain possibility. To reduce the computing time and also minimise the background level in the final hypernuclear missing mass spectrum, the event selection is necessary in the off line analysis. The main steps can be outlined as:

Beam TOF Hit time difference between BH1 and BH2 is used as a time-of flight to reject protons contaminating the beam.

TOF BH2 together with Tof is used as TOF detector. Time difference between BH2 and Tof is used to veto π^+ and protons from nuclear reactions.

ΔE The energy deposited inside the Tof depends on the particle type. It can be used as a ΔE detector to distinguish K^+ from π^+ and protons.

Tof and LC Consistency By requesting the correlation between hit segments of Tof and LC, the large scattering angle particles, which were originated from the background, can be eliminated.

Consistency between SDC3, SDC4 and Tof The particle hit position on Tof can be calculated from the SDC3 and SDC4 data. At the same time, the actual hit position can be obtained by Tof itself[2]. If the difference of these two positions is beyond a reasonable range, the event was rejected as a background particle.

The flow chart of the above process is shown in Fig. 3.1. The events that can pass these selections were processed with the procedure described in the next section.

[1] The protons from (π^+, p) reaction can cause trigger by emitting δ rays when the proton pass LC.

[2] The horizontal hitting position is just the position of the fired segment. The vertical hitting position can be calculated from the time difference between the two end of Tof scintillator.

Figure 3.1: Flow chart of the event selection.

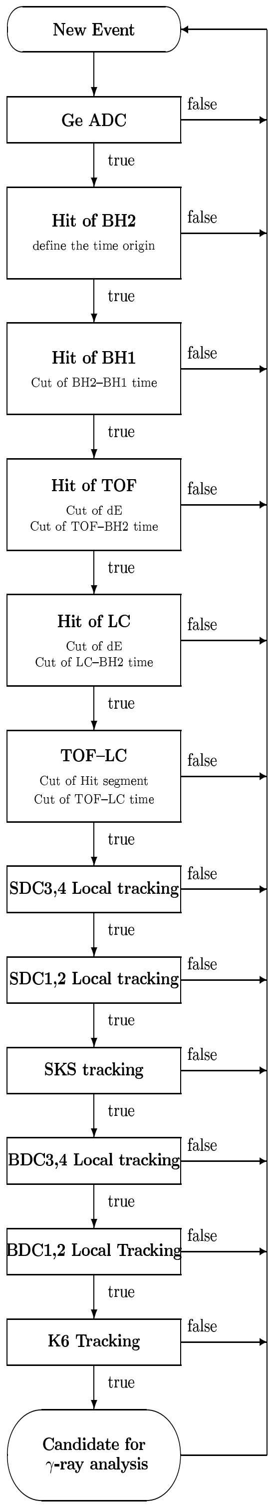

3.2.2 Kinematic Variable Determination

The kinematic variable calculation starts with the drift chamber analysis. The performance of the TDC used for the drift chambers were checked by two times calibration processes at the beginning and the end of the beam time. The time drift for each channel during one month is typically 200 psec. The effect to the drift length calculation is about 10 μm, while the spacial resolution of the drift chambers is about 300 μm (rms). Therefore, we can conclude that the TDC worked stable enough during the beam time. Then the beam-through run data were used to check the SKS momentum calibration and the position of the drift chambers. After these preparations, the tracking procedure was started.

Incident particle momentum reconstruction

First, a straight track was reconstructed with BDC1,2 by the least χ^2 fitting method. Then another straight track was built by the same procedure with BDC3,4 at the exit of QQDQQ. A transport matrix was used to link these two tracks. By requesting the following reduced χ^2 to be minimised, the momentum of the beam particle was determined.

$$\chi^2_{K6} \equiv \underbrace{\frac{1}{n-5}\sum_{i=1}^{12} H_i \left(\frac{P_i - f_i(\vec{X}_{in})}{w_i}\right)^2}_{\text{BDC1,2}} + \underbrace{\frac{1}{n-5}\sum_{i=13}^{24} H_i \left(\frac{P_i - g_i(\vec{X}_{out})}{w_i}\right)^2}_{\text{BDC3,4}}. \tag{3.3}$$

Here,

$$\begin{aligned} n &= \sum_{i=1}^{24} H_i \\ H_i &= \begin{cases} 1, & \text{if } i\text{th plane has a hit in the local track,} \\ 0, & \text{if } i\text{th plane has no hit in the local track,} \end{cases} \\ \vec{X}_{out} &= \mathcal{M}(\vec{X}_{in}, p), \end{aligned} \tag{3.4}$$

where P_i is the candidates for the hit position on the i-th plane of the drift chambers, which is obtained from the local tracks, and w_i is the spatial resolution of the i-th plane. $\vec{X}_{in}$ and $\vec{X}_{out}$ represent a direction of incident particles at the entrance and the exit of the magnet system, respectively. The hit position on the i-th plane for the fitted trajectories is denoted as $f_i(\vec{X}_{in})$ and $g_i(\vec{X}_{out})$. $\vec{X}_{out}$ is calculated from $\vec{X}_{in}$ through the 3rd-order transport matrix ($\mathcal{M}$) using a momentum (p) as a parameter [26]. For a multi-track event, all tracks were calculated and saved in order to keep good events as many as possible. A typical χ^2 distribution for K6 spectrometer is shown in Fig. 3.2. The measured momentum of the beam particle is plotted in Fig. 3.3

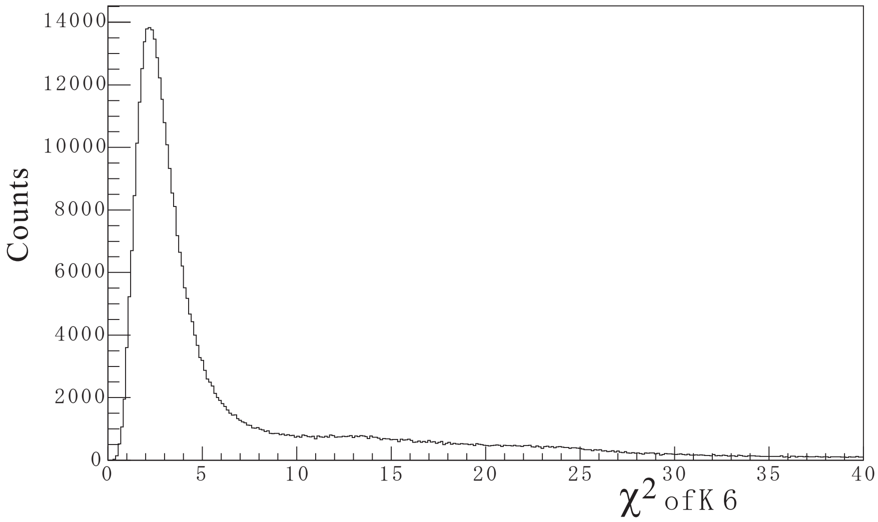

Figure 3.2: A typical χ^2 distribution of K6 tracking.

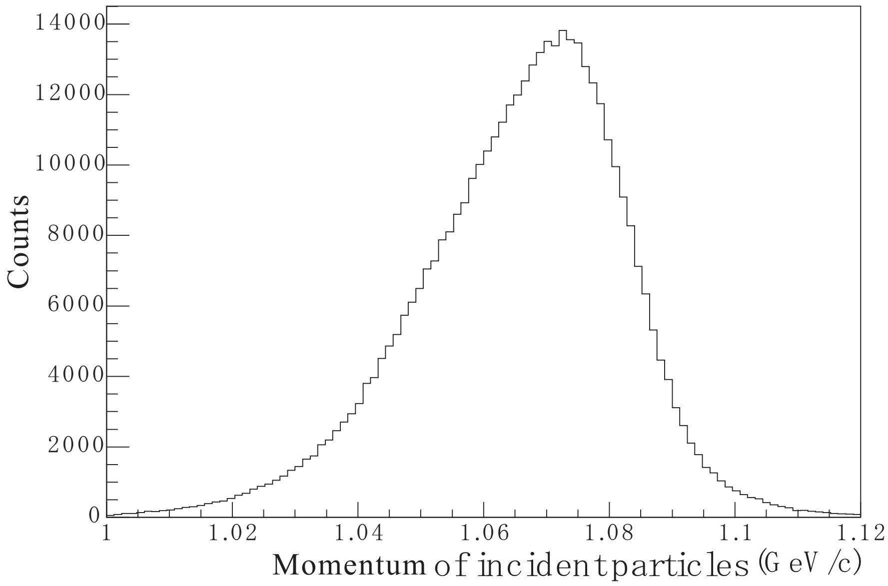

Figure 3.3: Beam momentum measured by the K6 beam line spectrometer.

Scattered particle momentum reconstruction

For the scattered particles, straight tracks were reconstructed at the entrance and at the exit of SKS by SDC1,2 and SDC3,4, respectively, with the least χ^2 fitting. Then the momentum was determined by requesting the following reduced χ^2 to be minimised

$$\chi^2_{SKS} \equiv \frac{1}{n-5}\sum_{i=1}^{n}\left(\frac{x_i^{tracking} - x_i^{data}}{w_i}\right)^2, \tag{3.5}$$

where n is the number of planes having hits, $x_i^{tracking}$ and x_i^{data} are the hit positions on the i-th plane in the tracking and the data, respectively, and w_i is the spatial resolution of the i-th hit plane. The path length of the trajectory was obtained. The Runge-Kutta method was used for the scattered particles instead of the transport matrix for the beam particles [31]. Again, all the tracks were saved and made combination with the incident particle tracks. A typical χ^2 distribution of SKS tracking is shown in Fig. 3.4. The calculated momentum for the scatted particles is shown in Fig. 3.5.

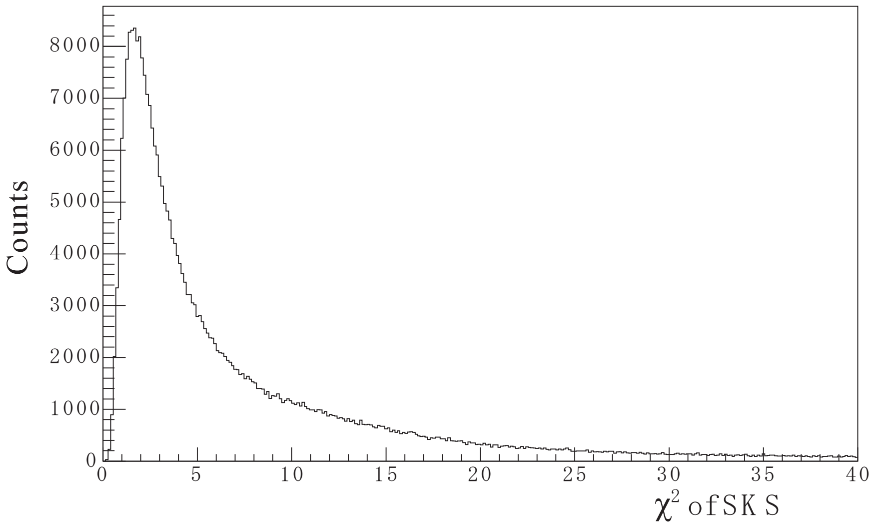

Figure 3.4: A typical χ^2 distribution of SKS tracking.

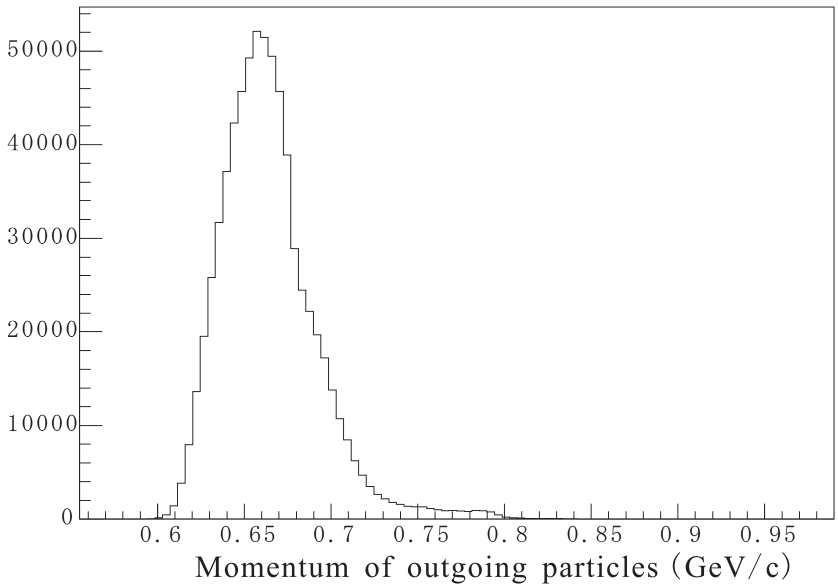

Figure 3.5: Momentum of scattered particles measured by SKS.

3.2.3 Results

After the determination of the kinematical variables, the results on the particle identification, vertex point of reactions, the missing mass, and so on are obtained.

Particle identification

After the tracking process is finished, the mass of the scattered particles can be calculated with

$$M_{out} = \frac{p}{\beta}\sqrt{1-\beta^2}. \tag{3.6}$$

At the beginning of analysis, the selection condition was set to be looser than usual to test the performance of the whole tracking procedure. Fig. 3.6 shows the results, from which we can clearly distinguish π^+ from K^+. The region between the red arrows is the accepted region.

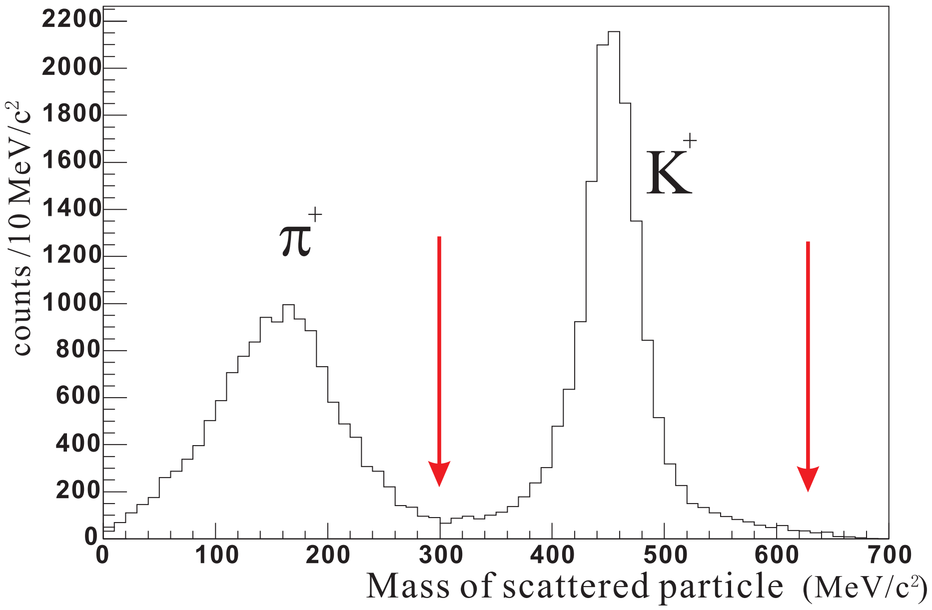

Figure 3.6: Mass of the scattered particles calculated by SKS.

Vertex selection

The vertex position was obtained from the incident π^+ track and the scattered K^+ track, which was determined by the K6 and SKS spectrometer, respectively.

The typical distribution of z coordinate of the vertex point is shown in Fig. 3.7. The left peak corresponds to the events in which π^+ reacted with BH2 material. The area between the red arrows are used as the accepted area. The vertex point distribution on the plane perpendicular to the beam direction is shown in Fig. 3.8.

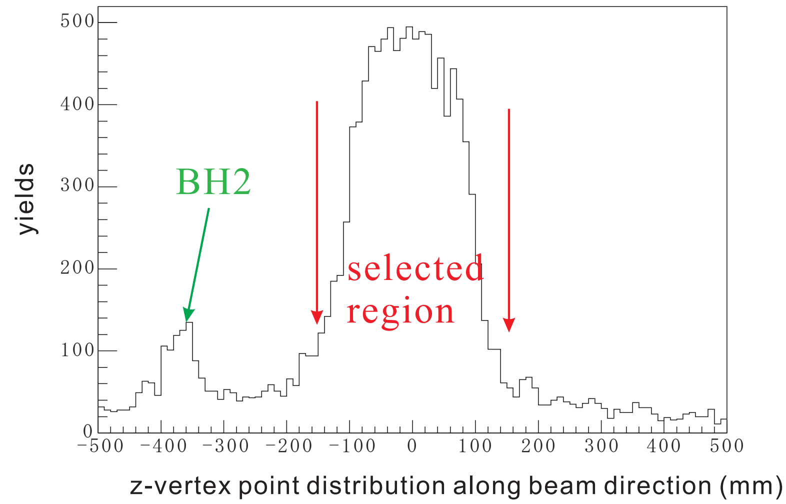

Figure 3.7: z-vertex distribution.

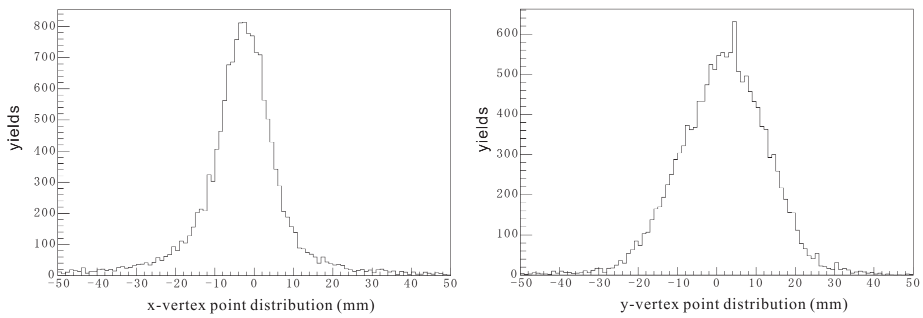

Figure 3.8: Left: vertex point distribution along x direction, right: vertex point distribution along y direction.

Energy loss and momentum correction

The energy loss due to Coulomb scattering inside the experimental target (material:$(CH_2)_n$, mass-thickness: 18.6 g/cm^2) need to be corrected. The path length of the particle inside the target was obtained from the vertex. Then energy loss of δE = 1.726 MeV (2.019 MeV) per centimetre was applied to π^+ (K^+).

Emperically, from the past SKS experiments, it is known that the momentum obtained from the tracking of SKS has corelation with incident angles of the scattered particles as shown in Fig. 3.9 from the ^{12}C reference target data. By the following correction formula

$$p_{K^+}^{corrected} = p_{K^+} + 17.0\left(\frac{dx}{dz}\right)_{K^+} + 21.0\left(\frac{dx}{dz}\right)_{K^+}^2 [\mathrm{MeV}/c], \quad (3.7)$$

the correlation can be effectively removed. Fig. 3.10 shows the result after this correction.

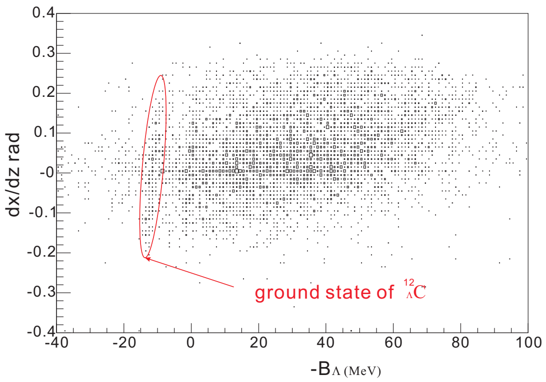

Figure 3.9: Correlation between dx/dz for SKS entrance angle (u$_{SKS}$) and the missing mass, (before correction).

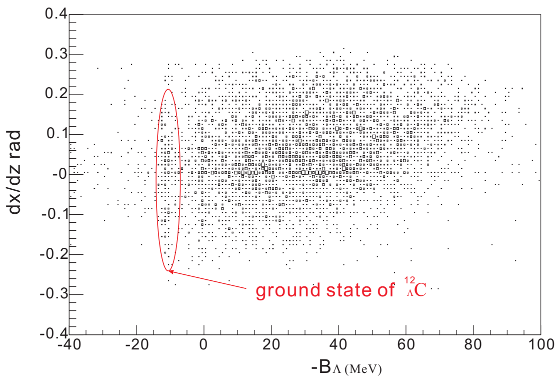

Figure 3.10: Correlation between dx/dz for SKS entrance angle (u$_{SKS}$) and the missing mass, (after correction).

Missing mass calculation

The missing mass defined in 3.1 is the key to identify which hypernuclear state was populated in the reaction. The missing mass was calculated with the corrected momentum. A typical distribution of the missing mass is presented in Fig. 3.11, which is compared to the result from KEK-E369 as shown in Fig. 3.12. The consistency of the result of the present experiment with the previous data is clearly seen. The result of the present experiment with the experimental $(CH_2)_n$ target is drawn in Fig. 3.14. The 2 cm ^{12}C result was also presented with a rescaled axis in Fig. 3.13 for comparison. The energy resolution in the present experiment is about 1.3 MeV (rms) and 4.8 MeV (rms) for 2 cm reference target and 20 cm experimental target, respectively.

It was found that the counts of the $^{12}_{\Lambda}$C ground state for experimental target are lower than an estimation based on the data of previous experiments at the same beam line. In previous experiments, the production rate of the ground state $^{12}_{\Lambda}$C hypernucleus with the (π^+, K$^+$) reaction was about 7 counts/(g/cm^2)/$10^9\pi^+$. However, the current analysis shows a result of about 2.4 counts/(g/cm^2)/$10^9\pi^+$. We are still trying to understand this inconsistancy.

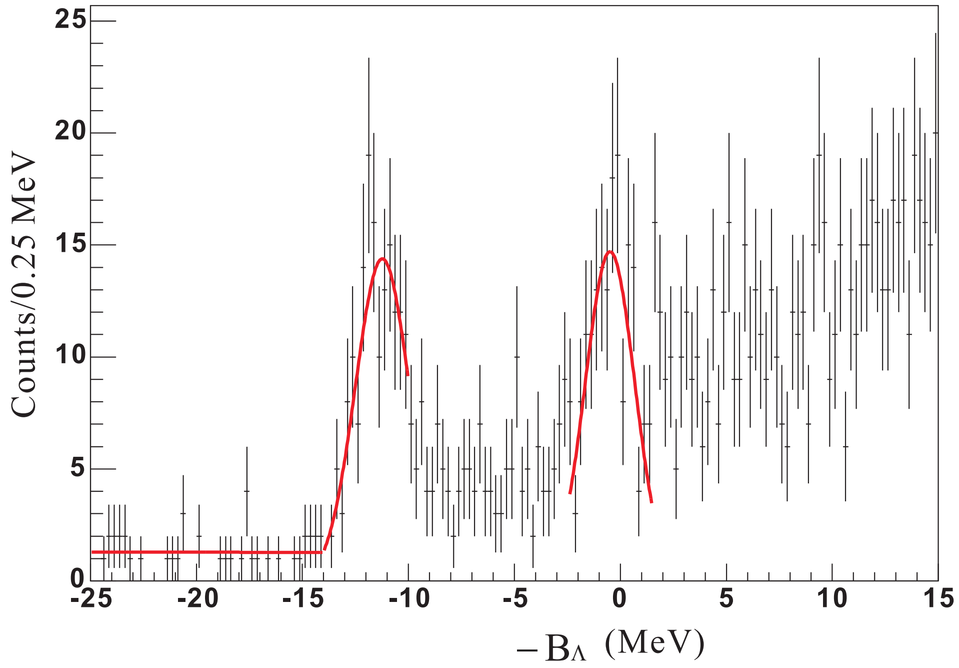

Figure 3.11: The binding energy spectrum for the reference target (2 cm ^{12}C). The two red curves corresponds to the #1 (Λ at the s-orbit) and #5 (Λ at the p-orbit) peak in the Fig. 3.12, respectively. The quoted errors are statistical only.

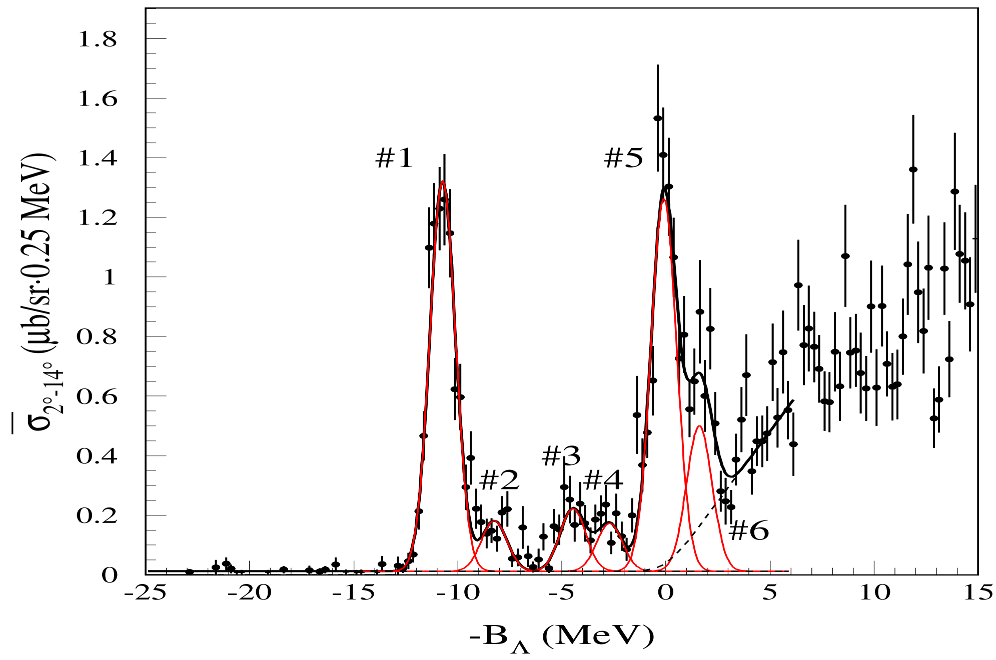

Figure 3.12: The binding energy spectrum for the ^{12}C target in the KEK-E369 experiment [6].

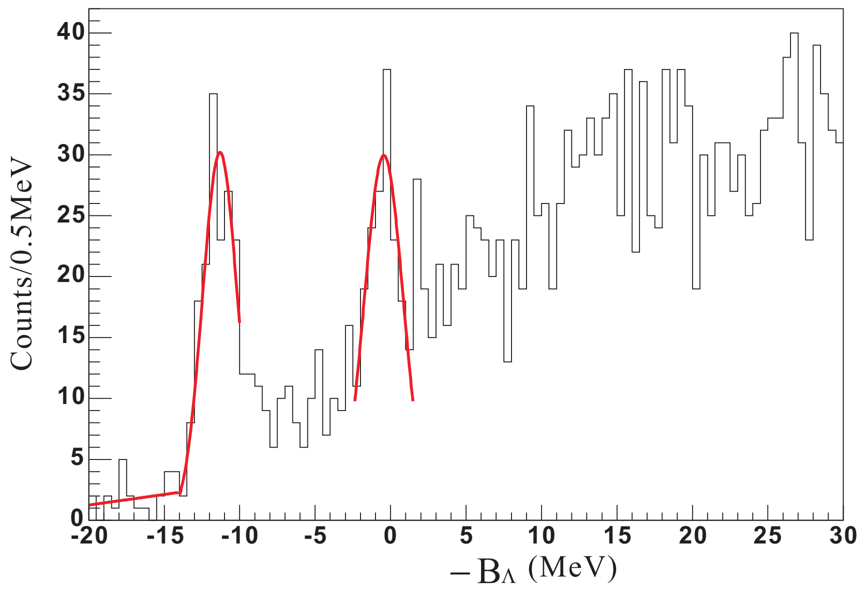

Figure 3.13: The binding energy spectrum for the reference target (2 cm ^{12}C).

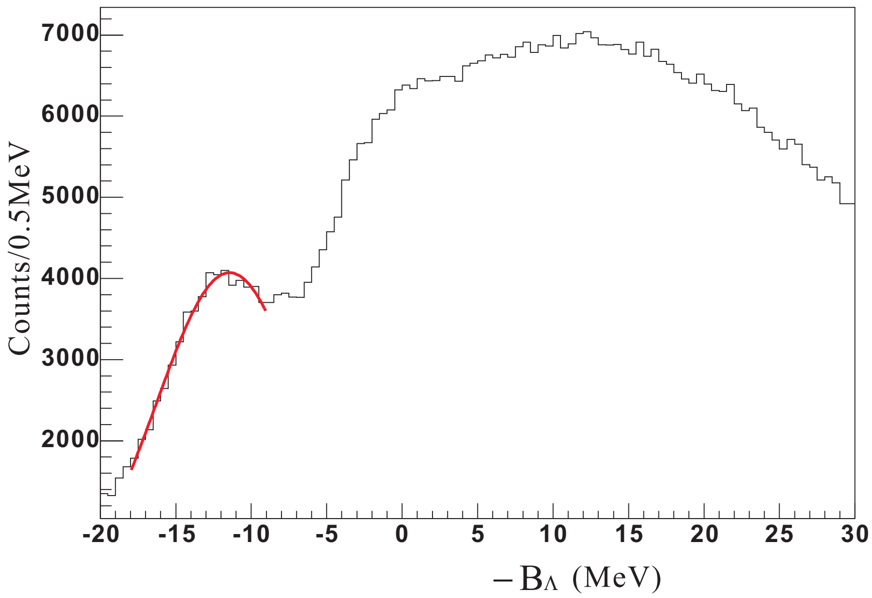

Figure 3.14: The binding energy spectrum for the $(CH_2)_n$ experimental target.

3.3 γ-ray Spectrum Analysis

Event selection

The first step in the γ-ray spectrum analysis is to veto background signals. The interested hypernuclear γ rays have a typical life time less than 10 ns. The TDC spectrum of a Ge detector with respect to the beam timing (BH2), which worked in a common-stop mode, has a typical distribution as shown in Fig. 3.15. The most probable region for true events to occur is in between the red arrows.

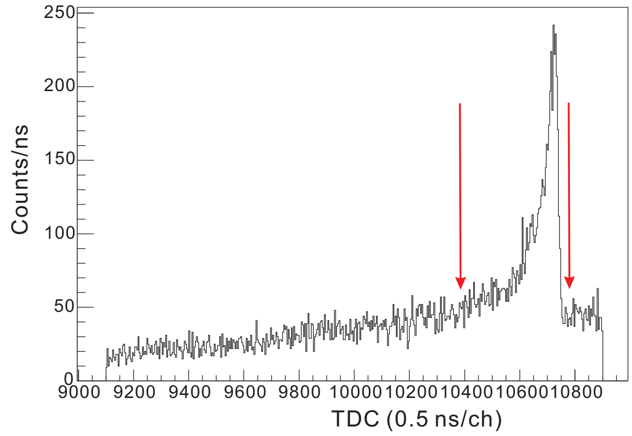

Figure 3.15: Typical TDC distribution of Ge detectors.

However, because the time resolution of Ge detector depends on the amplitude of the signal, the TDC distribution has a correlation with ADC, which can be seen from Fig. 3.16. The following function was used to describe this

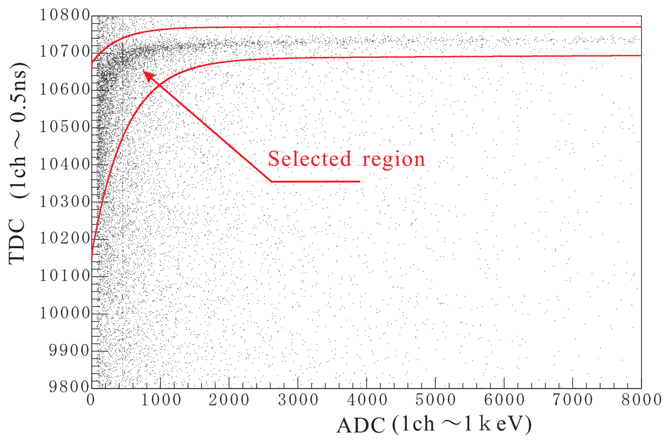

Figure 3.16: γ-ray TDC-ADC correlation from Ge.

correlation,

$$TDC = p0 \cdot e^{p1 \cdot ADC} + p2 + p3 \cdot ADC.$$

The region between the lower and upper curve in Fig. 3.16 was accepted as candidate events.

Ge energy calibration

The full range of γ-ray energy spectrum was set to be 9 MeV. To calibrate the Ge detectors in such a wide energy range, it is necessary to employ well known γ rays whose energy can cover this range. The γ-ray data with ^{152}Eu and ^{60}Co sources were acquired several times for calibration during one month beam time. The γ-ray energies from these sources are from 121 keV to 1408 keV. To calibrate the high energy part, the γ rays ($\sim$6 MeV) emitted from ^{16}O excited states as well as 2.75 MeV γ ray from a ^{24}Mg excited state were used. These excited ^{16}O were populated via β^- decay of ^{16}N produced by $^{16}\mathrm{O} + \mathrm{n} \rightarrow^{16} \mathrm{N} + \mathrm{p}$ reaction with oxygen in the BGO counters. The ^{24}Mg γ rays came from ^{24}Na which was produced probably from aluminium around the target. The γ rays used to calibrate Ge detectors are listed in Table 3.1.

Table 3.1: γ rays used for the energy calibration of Ge detectors

Source	γ-ray energy(keV)
^{152}Eu	121.78
^{152}Eu	244.70
^{152}Eu	344.28
e^+e^-	511.0
^{152}Eu	778.90
^{152}Eu	964.06
^{152}Eu	1085.84
^{152}Eu	1112.09
^{60}Co	1173.24
^{60}Co	1332.50
^{152}Eu	1408.01
^{24}Mg	2754.03
^{16}O (DE)	5101.63
^{16}O (SE[a])	5617.63
^{16}O	6128.63

[a]DE and SE stand for single photon escape and double photon escape, respectively.

A fourth order polynomial function was used to fit the calibration curve. Fig. 3.17 shows the fitting result. The performance of the Ge detectors during the beam-on and beam-off period is different because of the high counting rate caused by beam particles. The difference can be seen in Fig. 3.18. A shift about 1 keV toward the low energy end was also observed during the beam-on period. The energy resolution for all the Ge detectors add up (including add-back of clover Ge) was $\sim$5 keV (FWHM) for 1 MeV γ rays.

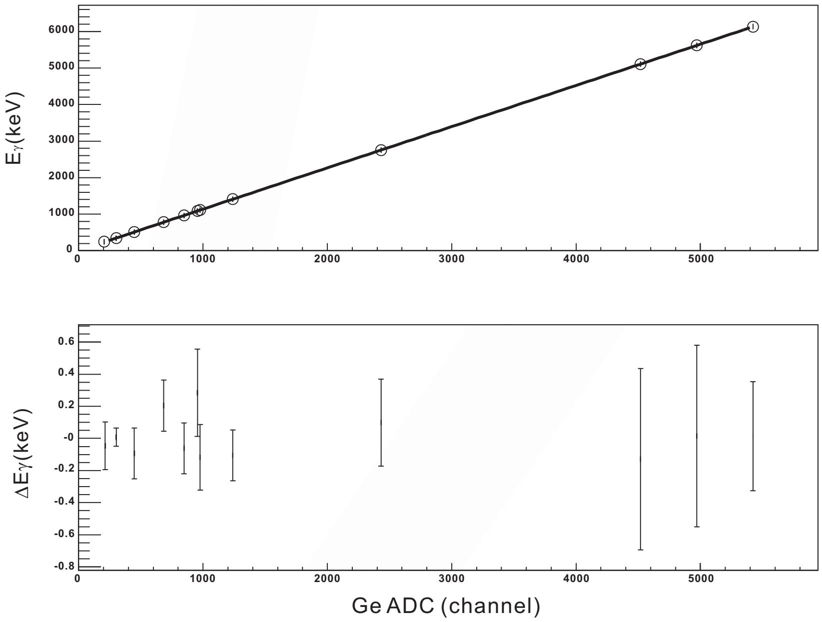

Figure 3.17: Upper: the calibration curve; lower: the deviation of the data from the calibration curve.

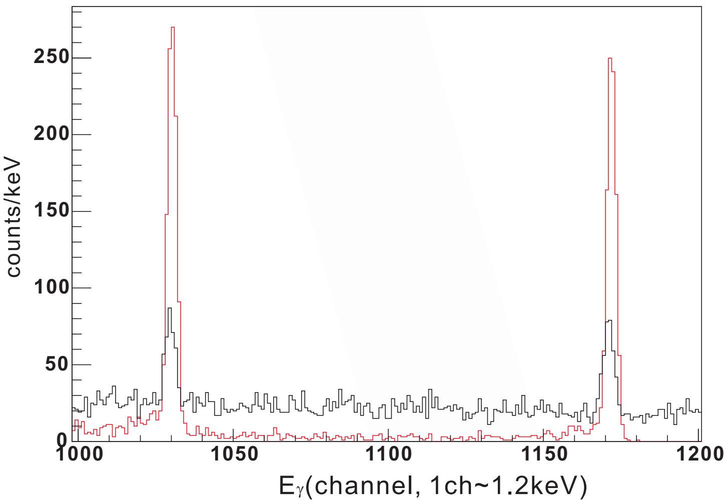

Figure 3.18: Red line is the γ-ray spectrum of a Ge detector during the beam-off period; the black line is the same spectrum acquired when the beam is on.

Clover Ge add-back effects

As introduced in the Chapter 2, the advantage of the clover Ge is the increase of photo-peak efficiency by adding back the signals of the four segments in one event. The add-back effects can be seen in Fig. 3.19. The data in Fig. 3.19 was from a ^{60}Co source. The full energy was increased by about 1.5 times while the Compton scattered events were decreased.

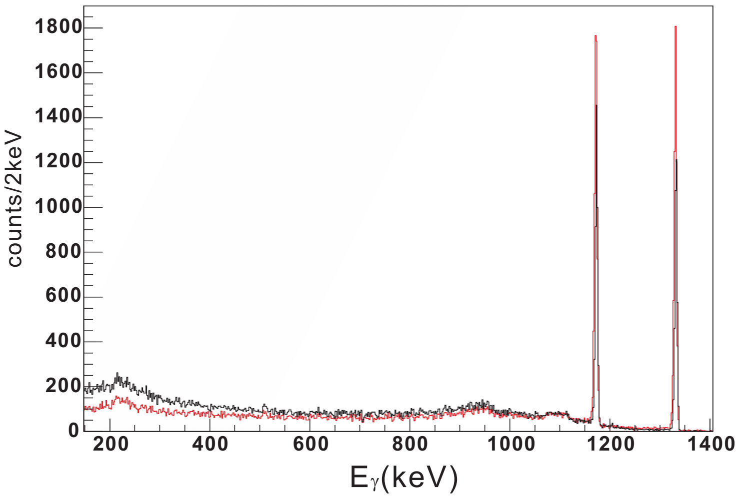

Figure 3.19: The effects of add-back in clover Ge detectors.

Ge efficiency

The photo-peak efficiency of the Ge detectors was measured with the ^{60}Co and ^{152}Eu sources whose intensities were known. The photo-peak efficiency as a function of γ-ray energy (100 keV $\sim$ 3000 keV) was measured and drawn in Fig. 3.20. The following function was employed to fit the curve

$$\text{Efficiency} = (exp(c1 + c2 \cdot E_\gamma) + c3 + c4 \cdot E_\gamma + c5 \cdot E_\gamma^2) \times c6. \tag{3.8}$$

Because the experimental target was 20 cm long, the sources were placed at three positions (two ends and the middle of the target) and the data were averaged to represent the real situation. The photo-peak efficiency of Hyperball2 with clover add-back is about 5.4% for 1330 keV γ rays. The photo-peak efficiency became lower than the measured value during beam on. This difference can be defined as

$$\text{Efficiency}_{relative} = \frac{\text{Counts of 1170 keV and 1330 keV } \gamma \text{ rays when beam was on}}{\text{Counts of 1170 keV and 1330 keV } \gamma \text{ rays when beam was off}},$$

where the 1170 keV and 1330 keV γ rays were emitted from the ^{60}Co pulser. It was found that Efficiency$_{relative}$ was about 54%.

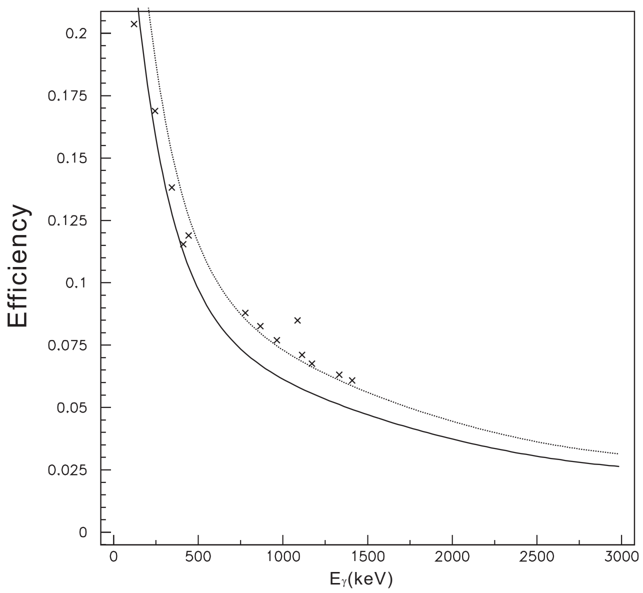

Figure 3.20: Photo-peak efficiency as a function of γ-ray energy. The $\times$ points are the data when the sources were placed at the center of the Hyperball. The dashed curve is the fitted curve for these points. The solid curve is the fitted curve for the averaged data acquired from three positions.

BGO suppression

To reduce the background in the γ-ray spectrum, it is necessary to apply the BGO suppression. In the case of the single Ge detector, if any one of the six BGO crystals was fired together with the Ge detector, the current event was rejected as a background event. For the Clover Ge, a more sophisticated method was used: only if any one of the four neighbour BGO and the segment surrounded by them were fired, the event was rejected. This is illustrated in Fig. 3.21.

The BGO gate width was determined to optimize the signal to noise ratio (S/N) and also signal square to noise ratio (S^2/N). In the current analysis, a known γ ray (1482 keV) emitted from ${}^{11}_{\Lambda}$B was chosen as the signal (S) The background of this γ-ray peak was used as the N. We started from 25 ns BGO gate width and increased with every 25 ns to 200 ns. The S/N and S^2/N value as a function of BGO gate width are drawn in Fig. 3.22 and Fig. 3.23. Based on these data, the BGO gate width was set to be 125 ns. The γ-ray spectrum with and without the BGO suppression are drawn together in Fig. 3.24. Some known peaks are marked with corresponding sources. Two peaks are assigned to be from ${}^{11}_{\Lambda}$B. The reasons for this assignment will be discussed in Chapter 4. The suppression factor, which is defined as

$$S_{factor} = \frac{\text{Counts without BGO suppresion}}{\text{Counts with BGO suppresion}},$$

is shown in Fig: 3.25, from which we can see that the Compton scattered events are suppressed more than the events which belong to the full energy peak.

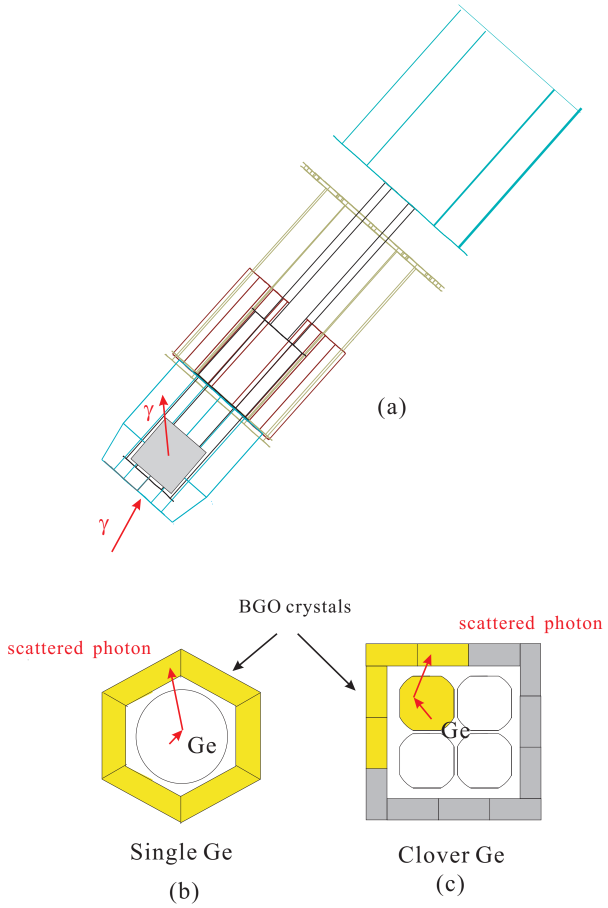

Figure 3.21: BGO suppression scheme: (a) the schematic view of a Compton scattered event; (b) the BGO suppression in the case of single Ge (all six BGO segments were used to veto scattered photons); (c) the case of clover Ge (Only the four yellow BGO were used to veto the scattered photons from the surrounded Ge segment).

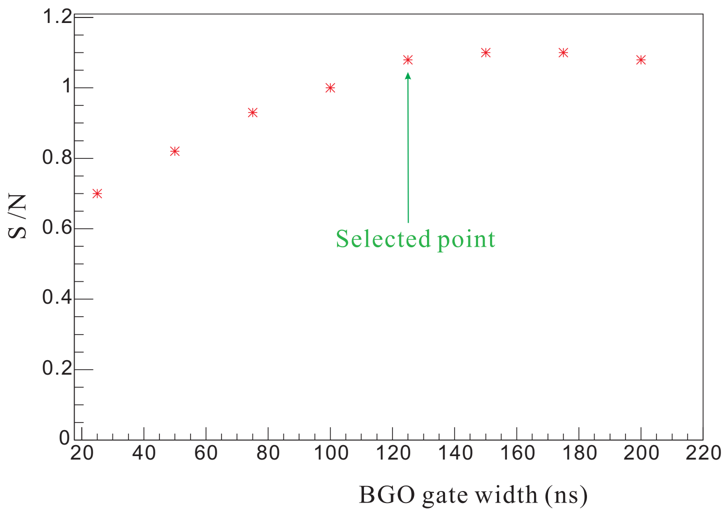

Figure 3.22: S/N ratio as a function of BGO gate width. S is the counts of the 1482 keV γ ray from $^{11}_{\Lambda}$B hypernucleus. N is the counts of background of this peak.

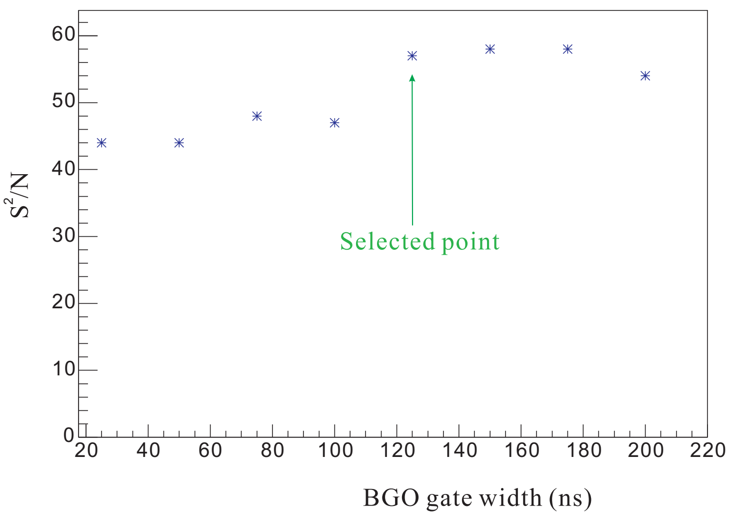

Figure 3.23: S^2/N ratio as a function of BGO gate width. S is the counts of the 1482 keV γ ray from $^{11}_{\Lambda}$B hypernucleus. N is the counts of background of this peak.

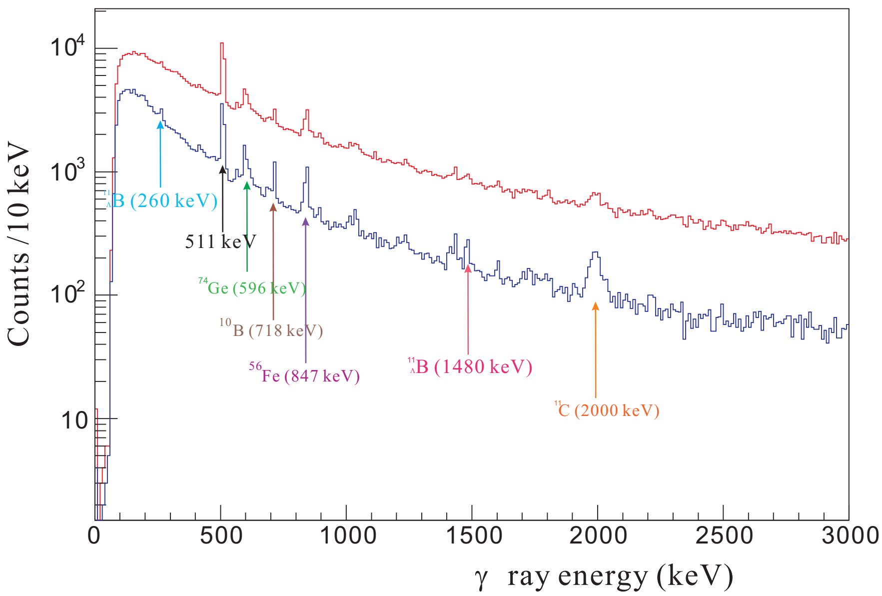

Figure 3.24: γ-ray spectrum with (blue curve) and without (red curve) BGO suppression.

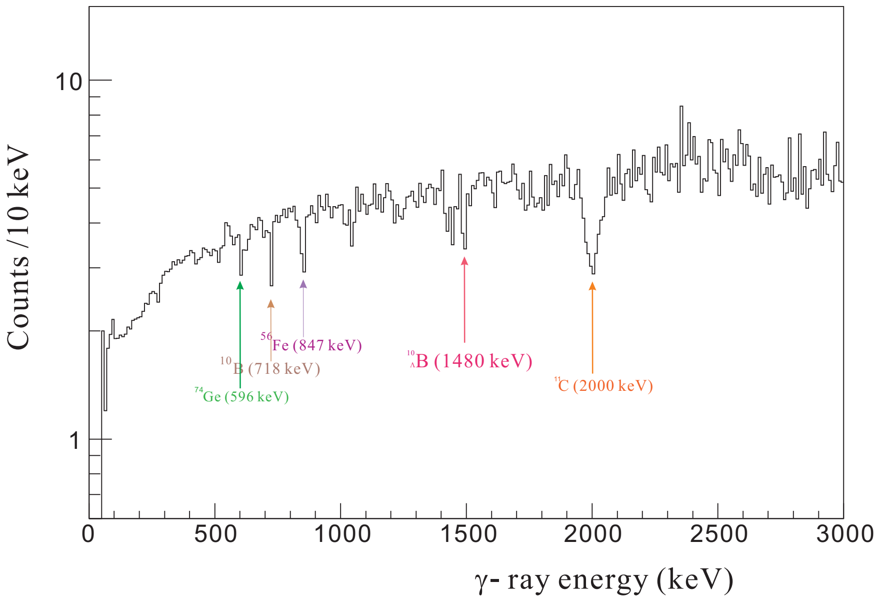

Figure 3.25: Suppression factor of BGO counters.

3.4 Doppler Shift Correction and Doppler Shift Attenuation Method

Doppler shift correction

The measured γ-ray energies are influenced by the motion of the parent nucleus. This effect is referred to as Doppler shift effect, which is schematicly shown in Fig. 3.26, where θ is the angle between the recoil momentum of the parent nucleus and the detector. β is the velocity of the parent nucleus.

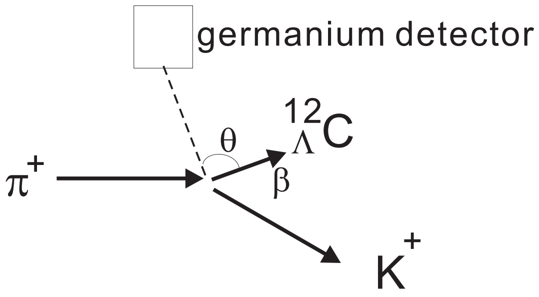

Figure 3.26: Schematic view of the Doppler shift effect.

The Doppler shift effect can be corrected by the following relation

$$E_{corrected} = E_{measured} \times \gamma(1 - \beta \cos\theta), \tag{3.9}$$

where the $E_{measured}$ is the energy measured by the detectors and the $E_{corrected}$ is the γ-ray energy when it is emitted from the parent nucleus who is at rest. In the present experiment, the momenta of the incident pions and outgoing kaons were measured one by one by the beam line spectrometer and SKS spectrometer, respectively. Thus the value and direction of β can be obtained for each event. One thing that need to be noticed is that the β obtained in this way is for the parent nucleus right after their population and not necessarily the value when they emit the γ rays. In another word, the Doppler shift correction requires that the lifetime of the EM transition is short enough to have a good result.

The uncertainty caused by the correction with the above equation can be estimated as following:

$$\Delta E_{corrected} = E_{measured}\beta\gamma \sin\theta\Delta\theta,$$

where we assumed that the main source of the uncertainty is from the uncertainty of θ. The uncertainty of θ is determined by two factors: the z-direction vertex resolution and the size of the Ge detectors. The z-direction vertex resolution is about 2 cm and the diameter of the Ge detectors (both single-type and clover-type) is approximately 7 cm. Thus $\Delta\theta$ is estimated to be $\pm 15^0$.

The typical value of the β of the populated hypernucleus is around 0.035. Consequently, we can have

$$\Delta E_{corrected} = 0.009 \times E_{measured}. \tag{3.10}$$

In the last step, the $\sin\theta$ was further assumed to be 1.

Doppler Shift Attenuation Method (DSAM)

The Doppler shift effect can also be employed to estimate the lifetime of the interested transitions. For example, if the lifetime is comparable with the stopping time of the recoiling parent nucleus inside the target medium, the measured γ-ray energy is Doppler broadened. So that the shape of the γ-ray peak is related with the lifetime and the stopping time of the parent nucleus. By adjusting the lifetime of the EM transitions as a parameter in the simulation to reproduce the measured peak shape, the lifetime of the corresponding γ rays can be obtained. It is also known as Doppler Shift Attenuation Method (DSAM).

Chapter 4

Result and Discussion

4.1 Selection of Hypernuclear States

The hypernuclear states were selected using the binding energy spectrum (B_Λ) at the beginning of the γ-ray spectrum analysis. Fig. 4.1[1] shows the different regions and the corresponding states. Based on Fig. 3.14 and the energy resolution (∼4.8 MeV in rms) in the present experiment, the binding energies corresponding to different hypernuclear states were defined to be:

$$s_\Lambda \ \text{ states} : -14 \ \text{ MeV} < B_\Lambda < -4 \ \text{ MeV}$$

$$p_\Lambda \ \text{ states} : -5 \ \text{ MeV} < B_\Lambda < 4 \ \text{ MeV}$$

$$\text{Highly excited states} : 1 \ \text{ MeV} < B_\Lambda < 9 \ \text{ MeV}$$

$$\text{Highly unbound region} : 15 \ \text{ MeV} < B_\Lambda.$$

"s_Λ" means states in which a Λ is populated in the s orbit of the hypernucleus, which is converted from a p-orbit neutron. As shown in Fig 1.6, four states (1_1^-, 2_1^-, 1_2^- and 1_3^-) are generated for different combinations between the nuclear core (^{11}C($3/2^-$, $1/2^-$)) and the s-orbit Λ. The 1_1^- state (ground state) is dominant because the (π^+,K$^+$) reaction selectively populates the spin-non-flip hypernuclear state. In the states described by the "p_Λ", a Λ is produced in the p orbit with a p-shell neutron. Three states (2_1^+, 2_2^+ and 0^+) are generated.

In the following sections, the γ rays from the p_Λ and highly excited states will be discussed first. Then the γ rays originated from the s_Λ states will be studied.

[1]The states mentioned here are calculated by Itonaga [17]. The corresponding energies are fine tuned based on the result of KEK-E369 and the present data.

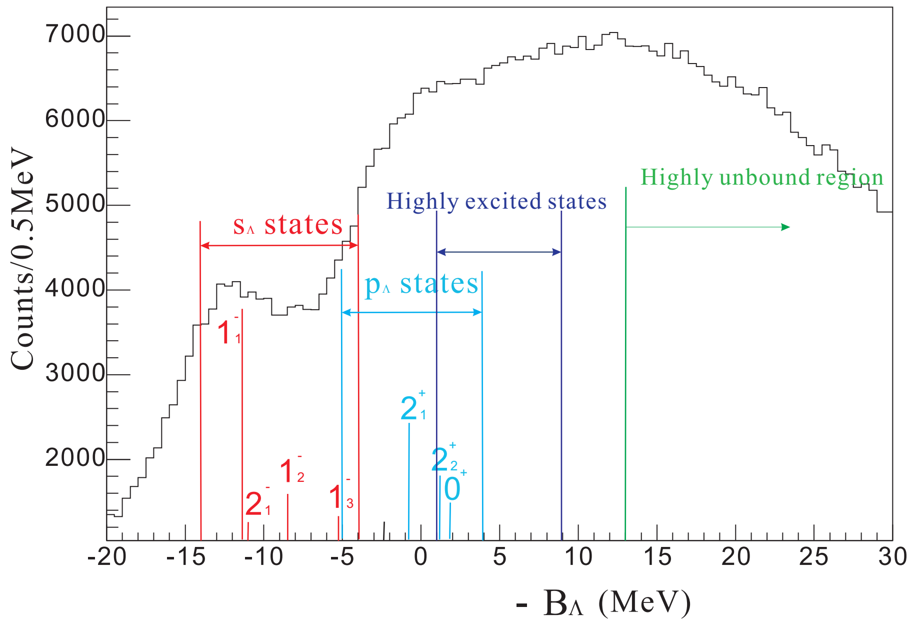

Figure 4.1: The ${}^{12}_{\Lambda}$C states and the corresponding regions in binding energy (-B_Λ).

4.2 γ rays from the p_Λ and Highly Excited States: ${}^{11}_{\Lambda}$B

As mentioned in Chapter 1, the ${}^{11}_{\Lambda}$B hypernucleus was generated via one proton emission from ${}^{12}_{\Lambda}$C if the Λ hyperon was in the p orbit or higher orbits. The ${}^{11}_{\Lambda}$B hypernuclei populated in excited states will further decay by EM transitions.

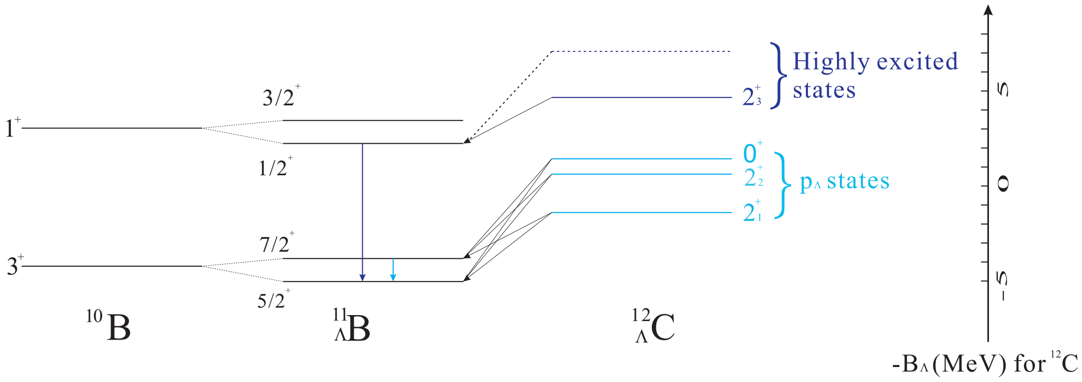

Figure 4.2: The states of ${}^{11}_{\Lambda}$B populated via one proton emission from ${}^{12}_{\Lambda}$C.

The ${}^{11}_{\Lambda}$B level scheme can be understood as a Λ coupling with a nuclear core (^{10}B) in the weak coupling scheme. Fig. 4.2 shows the schematic level diagram and the corresponding γ transitions from the excited states of ${}^{11}_{\Lambda}$B which are populated from the p_Λ or higher states of ${}^{12}_{\Lambda}$C.

Fig. 4.3 is the γ-ray energy spectra obtained for the different B$_\Lambda$ regions in the γ-ray energy range from 0 keV to 1 MeV. The γ-ray peak around 260 keV which is most dominantly populated in the p_Λ states region is identified as the $M1(\frac{7}{2}^+ \rightarrow \frac{5}{2}^+)$ transition. The evidence to support this assignment comes from a previous Hyperball experiment (KEK-518), from which it was found that the energy of the ${}^{11}_{\Lambda}$B$(1/2^+)$ state is too high to be populated by from the ${}^{12}_{\Lambda}$C$(0^+, 2^+_2, 2^+_1)$ states by proton emission. and there are no transitions in ${}^{11}_{\Lambda}$B other than $M1(\frac{7}{2}^+ \rightarrow \frac{5}{2}^+)$ from the p_Λ states. Fig. 4.4 is the γ-ray energy spectrum obtained for different states in the energy range from 1 MeV to 2 MeV. The γ-ray peak around 1480 keV from the highly excited states was also found in KEK-E518, which was assigned to be ${}^{11}_{\Lambda}$B$(\frac{1}{2}^+ \rightarrow \frac{5}{2}^+)$.

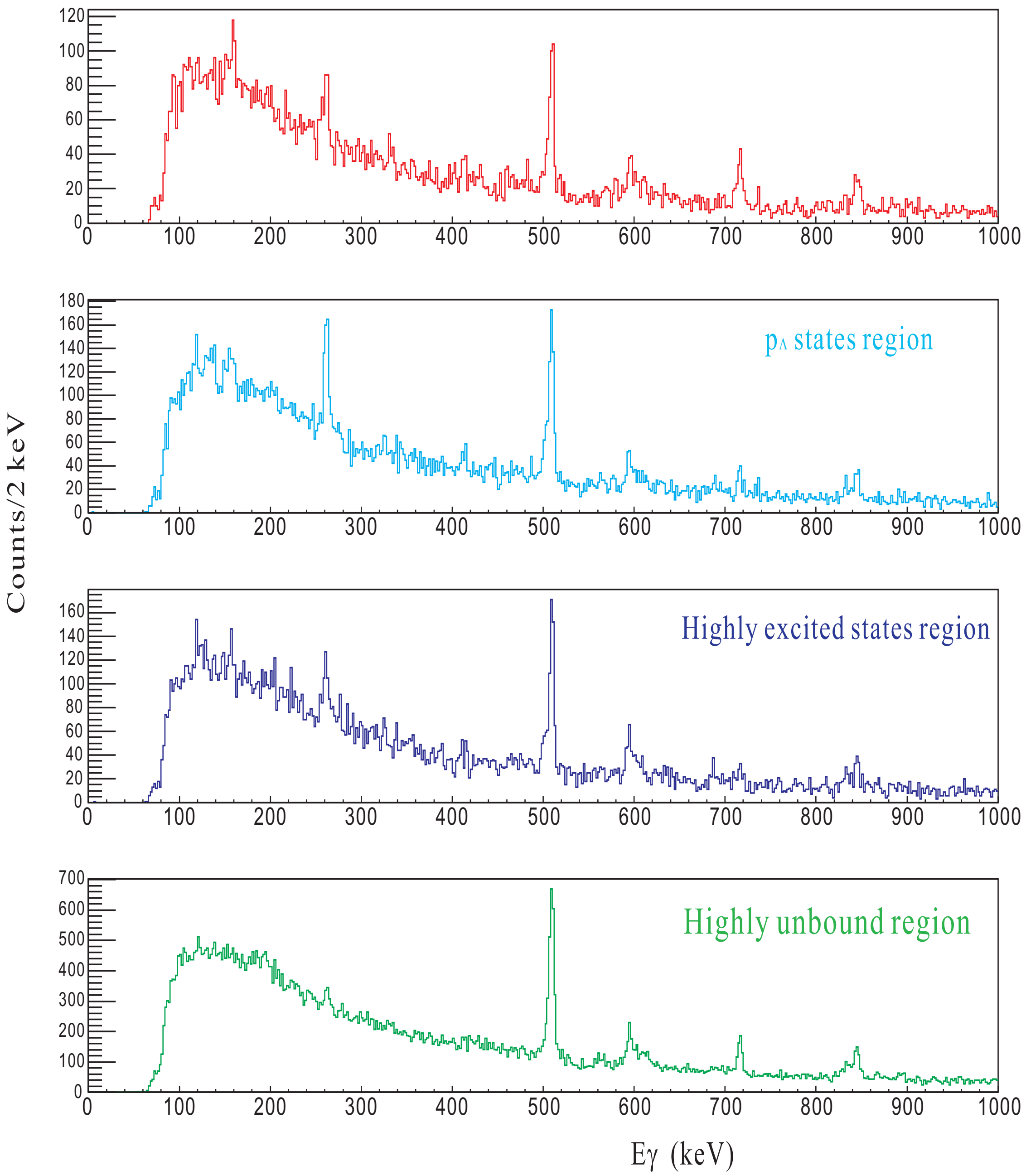

Figure 4.3: The γ-ray spectra (0 keV $<E_\gamma<$ 1000 keV) obtained for different B_Λ regions.

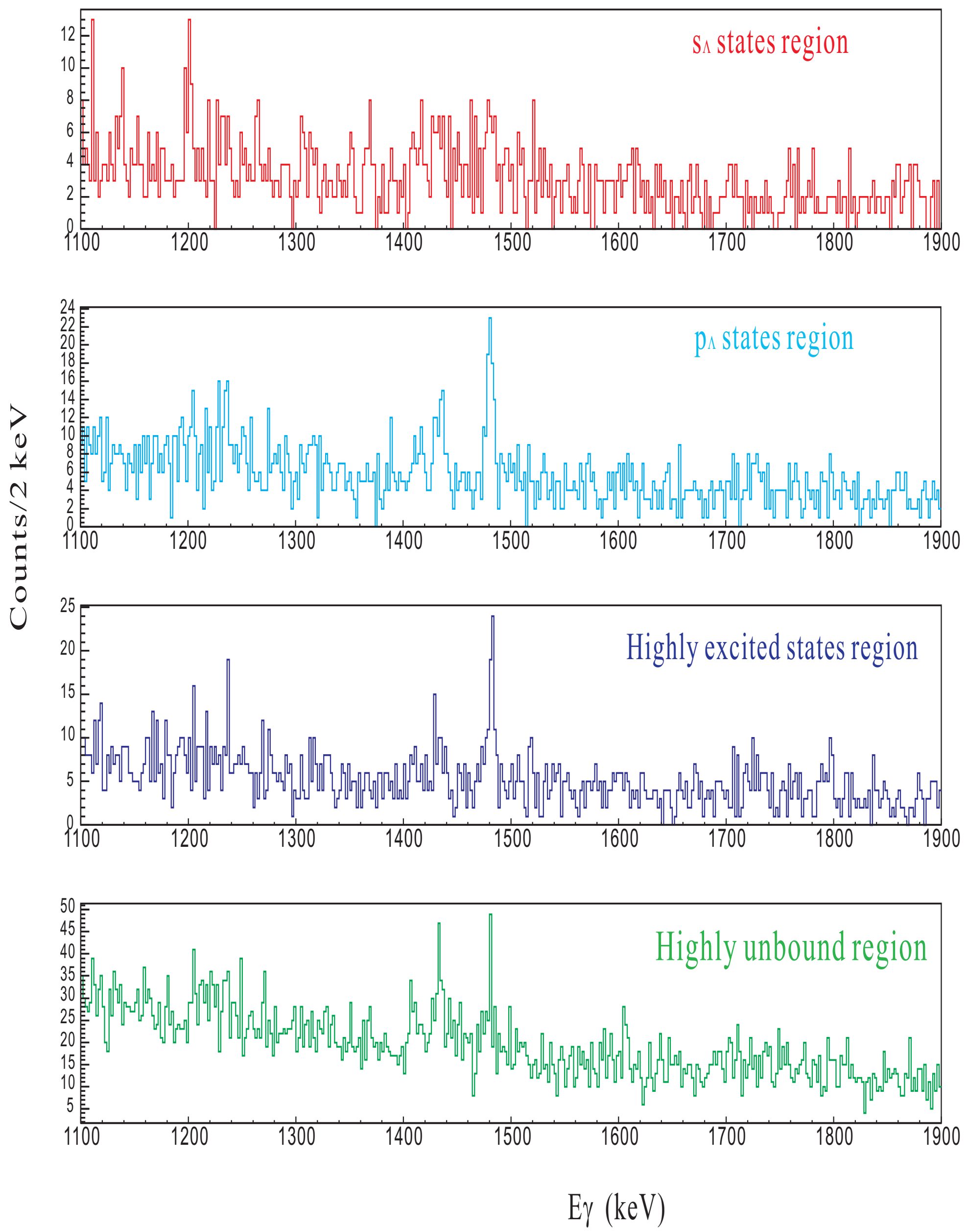

Figure 4.4: The γ-ray spectra (1100 keV $<E_\gamma<$ 1900 keV) obtained for different B_Λ regions.

Another support for this assignment is the variation of counts as a function of the selected hypernuclear mass ($-B\Lambda$), which is drawn in Fig. 4.5. The horizontal axis is the $-B_\Lambda$ value at the center of the selected hypernuclear mass region. It can be seen that most of the $\sim$260 keV and $\sim$1480 keV γ rays are in coincidence with the p_Λ and higher states.

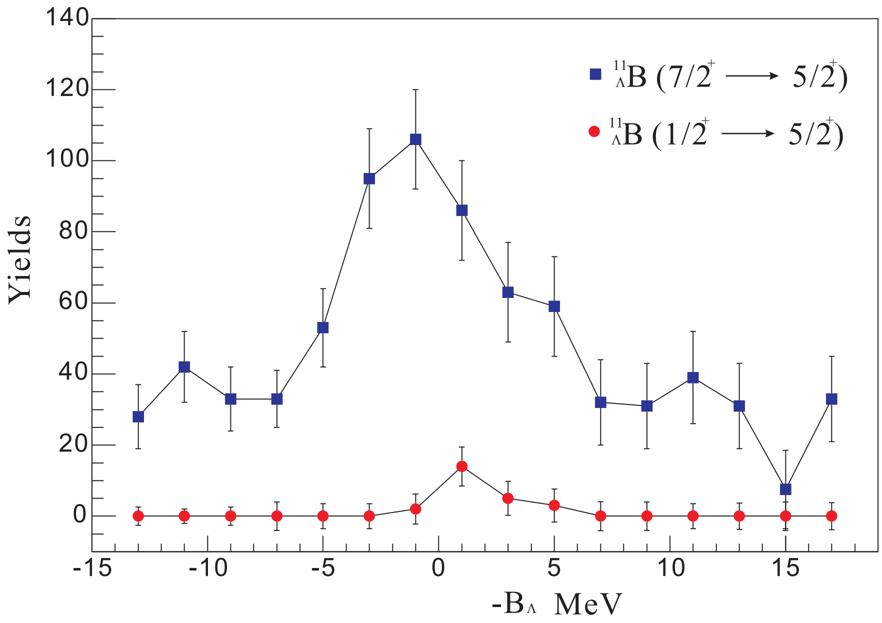

Figure 4.5: The counts of γ rays as a function of binding energy (-B_Λ)

These two γ-ray peaks were fitted with a Gaussian together a linear background function as drawn in Fig. 4.6 and Fig. 4.7. The results of these fitting are:
$E_\gamma({}^{11}_{\Lambda}\mathrm{B}(\frac{7}{2}^+ \rightarrow \frac{5}{2}^+)) = 261.6 \pm 0.24$ keV, and
$E_\gamma({}^{11}_{\Lambda}\mathrm{B}(\frac{1}{2}^+ \rightarrow \frac{5}{2}^+)) = 1481.7 \pm 0.7$ keV.
The fitted peak width (rms) for these two peaks are 2.2±0.2 keV and 3±0.7 keV, respectively, which are consistent with the γ-ray energy resolution of Hyperball2 in the current experimental conditions.

The $M1(\frac{7}{2}^+ \rightarrow \frac{5}{2}^+)$ transition energy calculated by Millener, using the parameters listed in Table 1.2, gives a value as
$E({}^{11}_{\Lambda}\mathrm{B}(\frac{7}{2}^+ \rightarrow \frac{5}{2}^+)) = 1.036\Delta + 2.453S_\Lambda + 0.039S_N + 3.330T = 475$ keV,
which is rather different from the measured value. More efforts in theoretical study are needed to understand this disagreement. The lifetime of $M1(\frac{7}{2}^+ \rightarrow \frac{5}{2}^+)$ transition with this energy is estimated to be about 7 ps by using the g_Λ value in the free space. The stopping time for the parent hypernucleus (${}^{11}_{\Lambda}\mathrm{B}$) in the current target medium is less than a few ps. Consequently, it is very difficult to apply Dopper Shift Attenuation Method (DSAM) to measure the life time of this $M1$ transition.

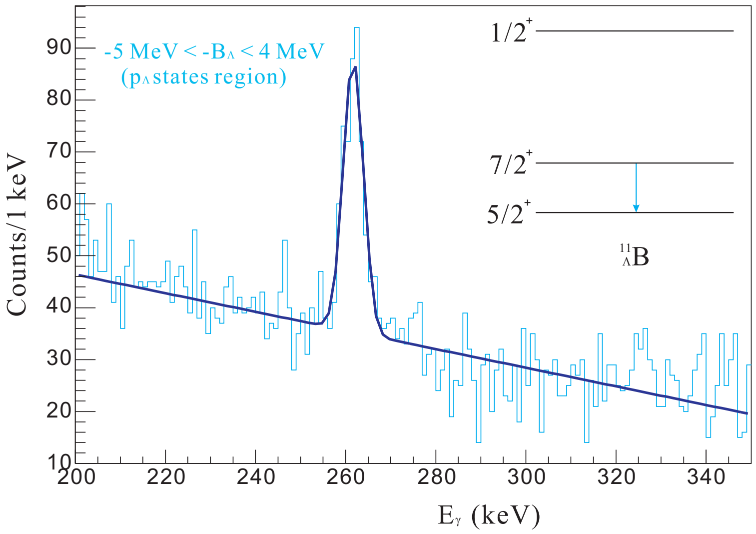

Figure 4.6: γ rays from ${}^{11}_{\Lambda}\mathrm{B}(\frac{7}{2}^+ \rightarrow \frac{5}{2}^+)$ transition.

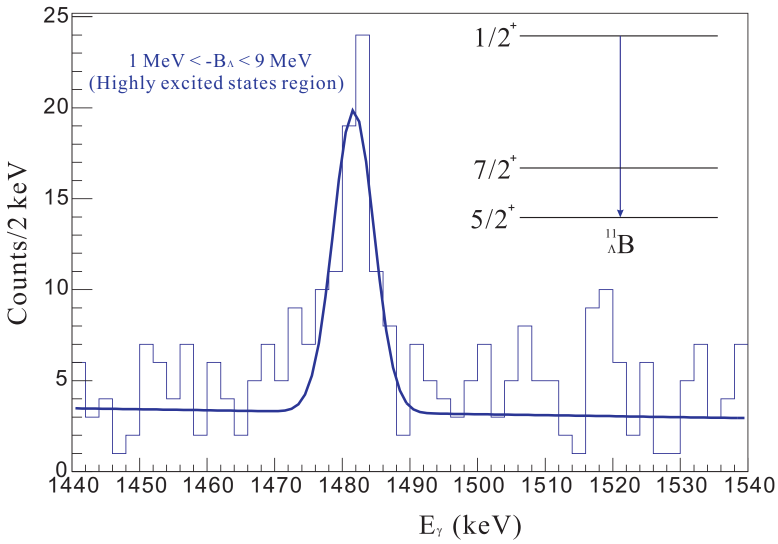

Figure 4.7: γ rays from ${}^{11}_{\Lambda}\mathrm{B}(\frac{1}{2}^+ \rightarrow \frac{5}{2}^+)$ transition.

4.3 γ rays from the s_Λ states: ${}^{12}_{\Lambda}$C

The ${}^{12}_{\Lambda}$C γ rays can be observed by gating the s_Λ states. The states and corresponding transitions from the excited states of ${}^{12}_{\Lambda}$C hypernucleus together with the ^{11}C nuclear core are shown in Fig. 4.8. The branching ratios (from Millener's calculation) and the level energies (from KEK-E369) are also mentioned [6].

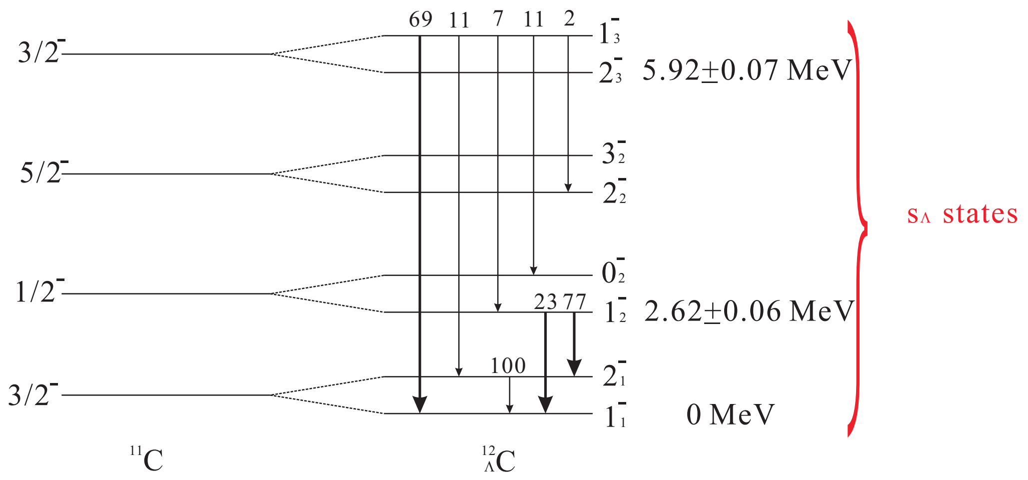

Figure 4.8: The states and possible transitions for the s_Λ states of ${}^{12}_{\Lambda}$C.

To investigate the transitions around 2.6 MeV, the γ-ray spectrum is rescaled and drawn in Fig. 4.9 and Fig. 4.10. Fig. 4.9 is the spectrum without applying the Doppler shift correction. Fig. 4.10 is the spectrum after applying the Doppler shift correction. A peak around 2650 keV has been observed clearly in the s_Λ states region of Fig. 4.10. This is consistent with our estimation: the stopping time of recoiling ${}^{12}_{\Lambda}$C inside $(CH_2)_n$ target was about 3 ps while the lifetime of 2.6 MeV $E1$ transition $(1^- \to 1^-, 2^-)$ γ rays is the order of 1 fs. So that the γ ray peak could be found after the Doppler shift correction. It is most likely that the observed transition is $(1^-_2 \to 2^-_1)$ because it has a relatively large branching ratio compared with $(1^-_2 \to 1^-_1)$ transition (It is calculated to be 3:1 in the weak coupling limit). No peak that corresponds to $(1^-_3 \to 1^-_1)$ transition is found in the current stage by checking the γ-ray spectrum in the expected energy range.

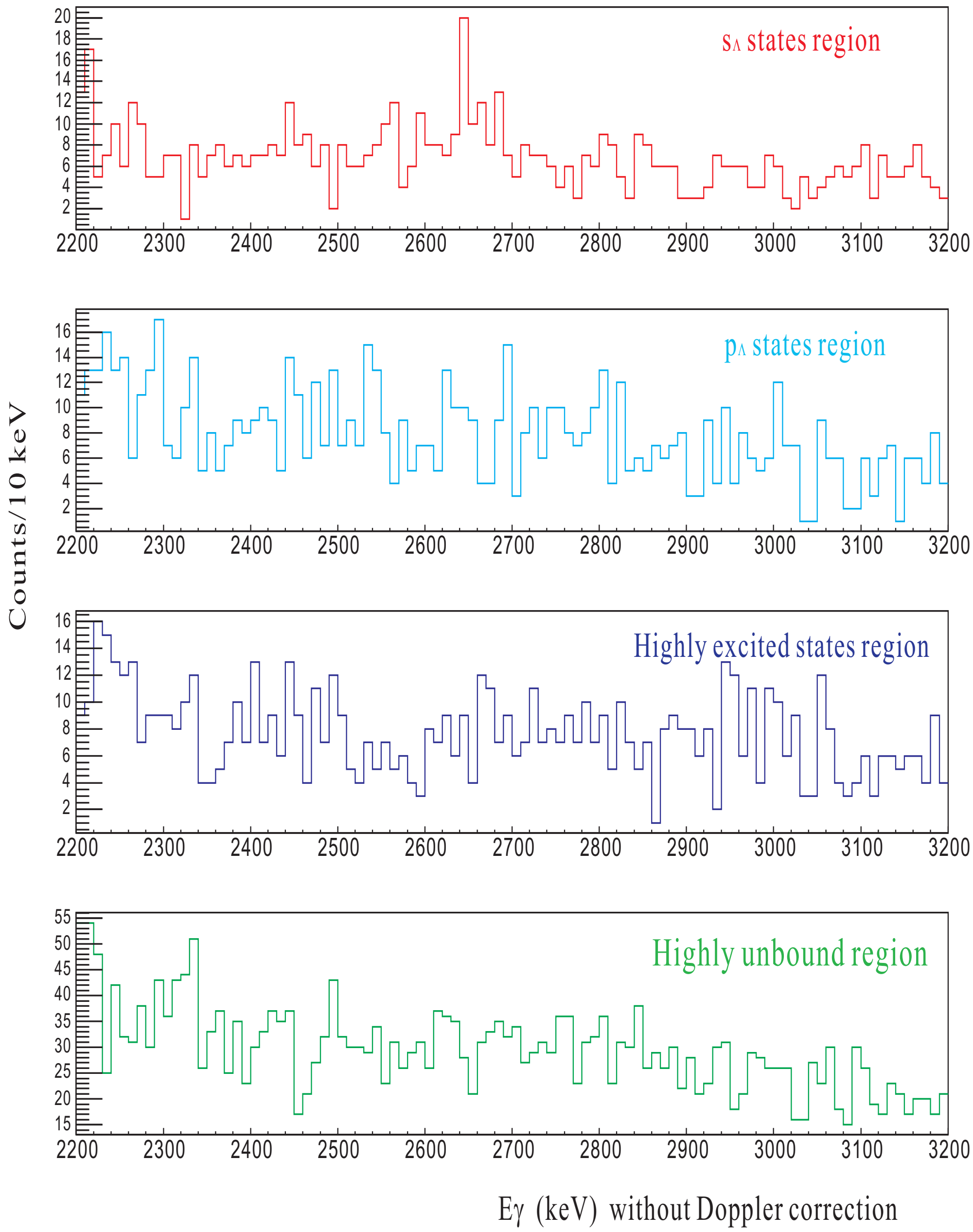

Figure 4.9: The γ-ray spectra (2200 keV $<E_\gamma<$ 3200 keV) obtained for different B_Λ regions without Doppler shift attenuation correction.

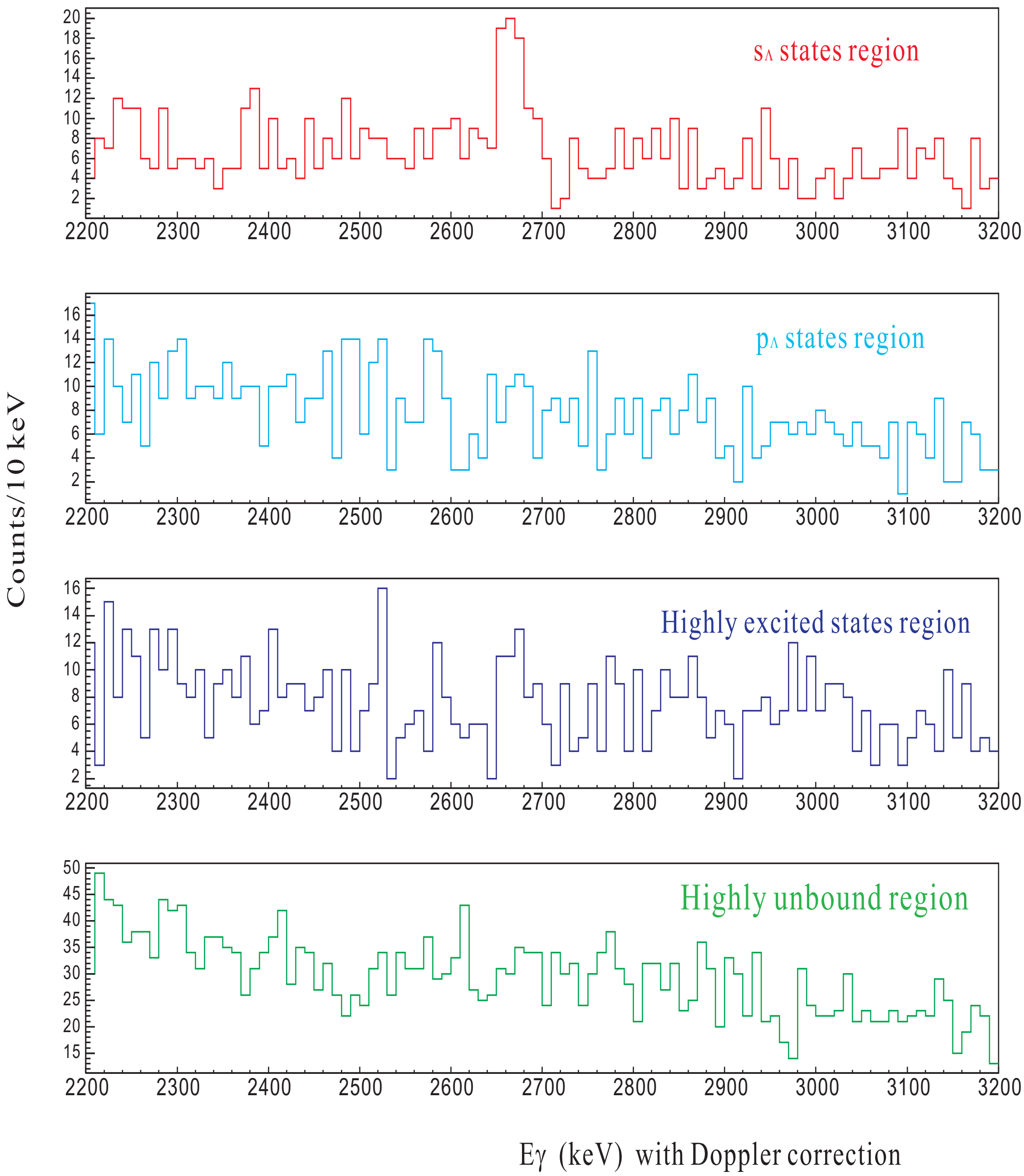

Figure 4.10: The γ-ray spectra (2200 keV $<E_\gamma<$ 3200 keV) obtained for different B_Λ regions with Doppler shift attenuation correction.

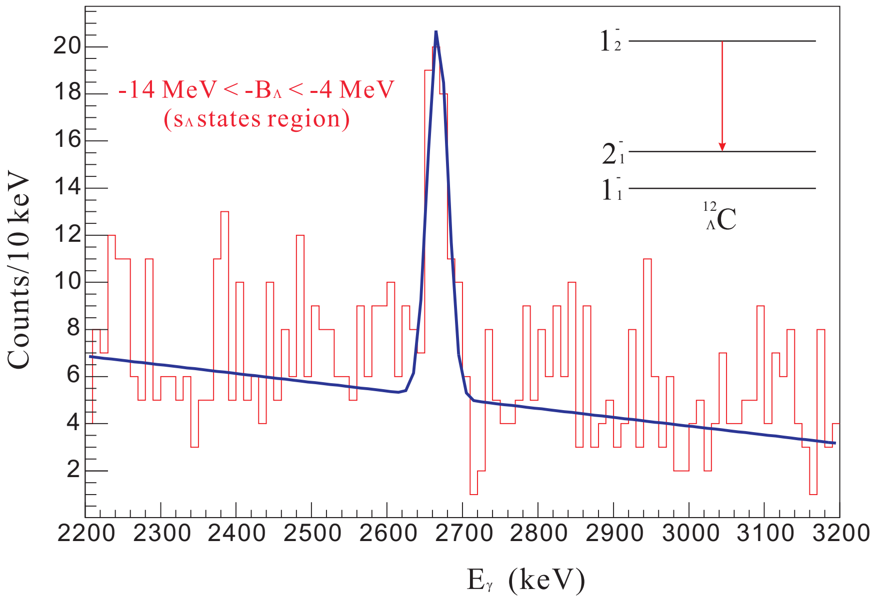

Figure 4.11: γ rays from $^{12}_{\Lambda}$C($1_2^- \rightarrow 2_1^-$) transition.

The Doppler corrected peak around 2660 keV was fitted with a Gaussian and a linear function. The fitted result shows that

$$E_\gamma(^{12}_{\Lambda}\mathrm{C}(1_2^- \rightarrow 2_1^-)) = 2667.3 \pm 2.8 \ \ \mathrm{keV}.$$

The fitted peak width (FWHM) is about 31.5±5.4 keV, which is consistent with the estimation from Eq.(3.10).

According to Millener's theoretical treatment, the γ-ray energy is:
$E_\gamma = \Delta E_{core} - 0.143\Delta - 0.363 S_\Lambda - 0.944 S_N + 2.762 T$,
where ΔE_{core} is the energy level spacing of ^{11}C($\frac{1}{2}^- \rightarrow \frac{3}{2}^-$) without the presence of the Λ. ΔE$_{core}$ is 2000 keV and the calculated numerical values for the interaction parameters (adjusted to $^{12}_{\Lambda}$C) are listed in Table 1.2. The calculated result is 2443 keV, in which the S_N term plays a dominant role. Compared with the experimental result, there is a difference of ~200 keV and it seems that an improvement of the theory is necessary. This inconsistency can be expressed in another way. This measured transition can also be used to derive the S_N parameter because it has the main contribution to this spacing. By assuming the numerical values of the other terms (Δ, S_Λ, T) given in Table 1.2, the S_N was determined to be −0.68 MeV, which is rather different from the previously accepted value (−0.4 MeV[2]). At the same time $^{11}_{\Lambda}$B($\frac{1}{2}^+ \rightarrow \frac{5}{2}^+$) (1482 keV) transition also gives a large S_N value as −0.9 MeV [15]. These two results may suggest that we need to include more effects to understand the ΛN interaction from the hypernuclear structure.

The ground state doublet transition ($M1(2_1^- \rightarrow 1_1^-)$) was investigated by checking the low energy part of the γ-ray spectrum for the s_Λ states region. One candidate peak for this spin-flip $M1$ transition was found as shown in

[2] This value can reproduce the $^{13}_{\Lambda}$C($\frac{3}{2}^+ \rightarrow \frac{1}{2}^+$) and $^{16}_{\Lambda}$O($1^- \rightarrow 1^-$) transitions very well.

Fig. 4.12. By assuming this transition is purely from the cascade transition

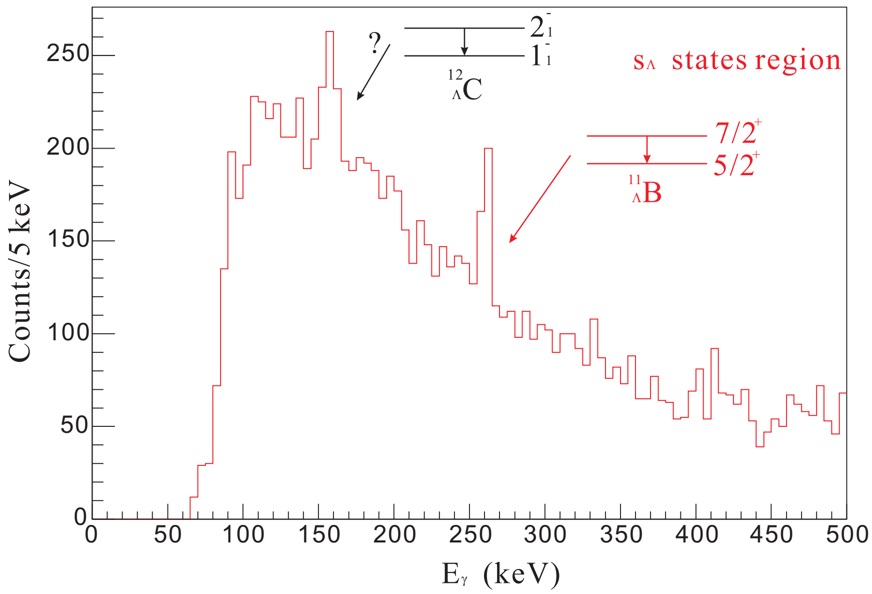

Figure 4.12: Candidate for the $^{12}_{\Lambda}\mathrm{C}(2_1^- \to 1_1^-)$ transition.

after $^{12}_{\Lambda}\mathrm{C}(1_2^- \to 2_1^-)$, and considering the energy-dependence of the photo-peak efficiency, the counts of events corresponding to the γ-ray peak around 150 keV should be about five times more than the counts in the 2667 keV peak, which was found to be 40. However, the counts of the 150 keV peak is about 170. It may be explained by including the competition from the weak decay etc. More analysis needs to be done before we can give a definite conclusion.

Chapter 5

Summary

The present experiment (KEK-E566) was carried out to study the precise structure of ${}^{12}_{\Lambda}$C and ${}^{11}_{\Lambda}$B hypernuclei by γ-ray spectroscopy technique. To test the universality of the experimentally determined parameters on the strengths of the ΛN spin-dependent interactions, which is based on a shell model calculation in a weak coupling scheme is also a motivation of the current experiment. In particular this experiment enables us to investigate the effect of the ΛNN three body interaction to p-shell hypernuclei. To measure the g-factor of a Λ hyperon in a nucleus is also a goal of this experiment.

The ${}^{12}_{\Lambda}$C was populated with the (π^+, K$^+$) reaction, which is characterized by its large momentum transfer. The ${}^{11}_{\Lambda}$B was produced via one proton emission from ${}^{12}_{\Lambda}$C when the Λ was generated in the p or higher orbits. A magnetic spectrometer system (beam line spectrometer and SKS spectrometer) was employed to identify the production of particular hypernuclear states. A germanium detector array (Hyperball2) worked in conjunction with the magnetic spectrometer to detect the γ rays from the hypernucleus.

In the current analysis stage, three γ-ray peaks were confirmed to be emitted from the hypernucleus of interest. They are:

$$ {}^{11}_{\Lambda}\mathrm{B} : E_\gamma(7/2^+ \to 5/2^+) = 261.6 \pm 0.24 \ \ \mathrm{keV}, $$

$$ {}^{11}_{\Lambda}\mathrm{B} : E_\gamma(1/2^+ \to 5/2^+) = 1481.7 \pm 0.7 \ \ \mathrm{keV \ and} $$
$$ {}^{12}_{\Lambda}\mathrm{C} : E_\gamma(1^-_2 \to 2^-_1) = 2667.3 \pm 2.8 \ \ \mathrm{keV}. $$

The 1482 keV γ ray was first found in a previous experiment (KEK-E518). The 262 keV γ ray was also observed in that experiment but the spin assignment was not given. In the present experiment, the spin assignment of 262 keV peak was successfully done by gating the p_Λ states of ${}^{12}_{\Lambda}$C in the binding energy spectrum. The 2667 keV γ ray was first time detected in our experiment. Theoretical predictions for the 262 keV and 2667 keV peaks are diviated by $\sim$200 keV from the experimental value for both of them. Another γ-ray peak around 180 keV was found as a candidate for the ${}^{12}_{\Lambda}$C ground state doublet transition. However, more analysis is necessary before we draw a definite conclusion.

Another task in the next step of analysis is to understand the loss of events. From previous experiments performed at the same experimental facility (K6 at KEK), it was found that the production rate of the ground state ${}^{12}_{\Lambda}$C hypernucleus with the (π^+, K$^+$) reaction was about 7 counts/(g/cm^2)/10$^9\pi^+$. However, the current analysis shows a result of about 2.4 counts/(g/cm^2)/10$^9\pi^+$. Thus solving of this problem may bring us more counts of the hypernuclear γ rays and, hopefully, more interesting results can be discovered.

Acknowledgements

First of all, I would like to take this opportunity to express my appreciation to my supervisor, Prof. Tamura, who provided me such a good opportunity to study in this top class university and prepared a very comfortable living conditions for me. Prof. Tamura also taught me many things that were not written in a text book. Particularly, I learned from him how to think and work like a Physicist. Also his patience and hard working give me a good example to follow.

I would like to say thank you to my group members. Dr. Koike taught me many experimental skills hand by hand from the beginning of my study. Dr. Miura shared with me many cherishable experiences he acquired during his study. Dr. Ukai let me know how to work precisely and how to have a clear image behind phenomena. Ms. Kinoshita and Mr. Shirotori are very helpful both in experiment and discussion. And also Dr. Miwa gave me many hints on analysis and encouraged me to finish the writing of this dissertation.

I am also grateful to Prof. Hashimoto's group, expecially Asistant Prof. Fujii and Asistant Prof. Kaneta. Fujii-san matained a very good computer system to make the analysis of our experiment feasible. Kaneta-san shared his time and knowledge with me so that I am always benefited from our discussions.

I acknowledge the referees of the present thesis, Prof. Tamura, Prof. Hashimoto, Prof. Inoue, Prof. Kobayashi, Prof. Nakamura and Prof. Maeda for giving me invaluable comments.

Finally, I would like to express my gratitude to our collaborators at KEK, Prof. Takahashi, Mr. Takahashi, Mr. Nakajima etc. for their hard working and effective cooperation on experiment.

References

[1] M. Danysz *et al.*, Phil. Mag. **44** (1953) 348.

[2] B. Povh, K. Rith, C. Scholz, F. Zetsche: *Particle and Nuclei* (Springer, Verlag, Berlin, Heidelberg, 1995)

[3] D. H. Davis, Nucl. Phys. **A 547** (1992) 369c.

[4] B. Povh, Prog. Part. Nucl. Phys. **5** (1981) 245.

[5] R. E. Chrien, Ann. Rev. Nucl. Part. Sci. **39** (1989) 113.

[6] H. Hotchi, Doctor Thesis of Graduate School, University of Tokyo

[7] R. H. Dalitz:*Nuclear Interactions of the Hyperons* (Oxford University Press, Amen House, London E.C. 4, 1965)

[8] A. Bamberger *et al.*, Nucl. Phys. **B60** (1973) 1.

[9] H. Tamura *et al.*, Phys. Rev. Lett. **84** (2000) 5963.

[10] D.J. Millener *et al.*, Phys. Rev. C **31** (1985) 499.

[11] D.J. Millener, Nucl. Phys. A **691** (2001) 93c.

[12] H. Akikawa *et al.*, Phys. Rev. Lett. **88** (2002) 082501.

[13] M. Ukai *et al.*, Phys. Rev. Lett. **93** (2004) 232501.

[14] M. Ukai *et al.*, Phys. Rev. C **73** (2006) 012501.

[15] Y. Miura, Doctor Thesis of Graduate School, Tohoku University

[16] D.J. Millener, private communucation

[17] K. Itonaga, T. Motoba, O. Richter, and M. Sotona, Phys.Rev. C**49** (1994)

[18] H. Hotchi *et al.*, Phys. Rev. C**64** (2001)

[19] R.E. Chrien *et al.*, Phys. Rev. C **41** (1990) 1062.

[20] Y. Akaishi *et al.*, Phys. Rev. Lett. **84** (2000) 3539.

[21] H. Tamura *et al.*, Proposal for KEK-E566.

[22] B. F. Gibson *et al.*, Phys. Rev. C **6** (1972) 741.

[23] A. de-Shalit, Phys. Rev. **122** (1961) 1530.

[24] H. Bandō *et al.*, Int. J. Mod. Phys. A **A 5** (1990) 4021.

[25] H. Bandō *et al.*, Phys. Rev. C **39** (1989) 587.

[26] T. Hasegawa, Doctor Thesis of Graduate School, University of Tokyo

[27] K. H. Tanaka *et al.*, Nucl. Phys. A **450** (1986) 533c.

[28] T. K. Ohska *et al.*, IEEE Trans. Nucl. Sci. **33** (1986) 98.

[29] T. Miyoshi *et al.*, Phys. Rev. Lett. **90** (2003) 232502.

[30] G. F. Knoll: *Radiation Detection and Measurement* (John Wiley&Sons, New York, Chichester, Brisbane, Toronto, Singapore, 1989)

[31] J. Myrheim *et al.*, Nucl. Instr. Meth. **160** (1979) 93.

Appendix A

Two-body ΛN effective interaction

Appendix A gives an introduction to the theoretical treatment for the two-body effective ΛN interaction. The level energies in hypernucleus can generally be expressed as

$$E = \left\langle \Psi_{HY} \left| \frac{1}{2} \sum_{i,j} H_{i,j} \right| \Psi_{HY} \right\rangle, \tag{A.1}$$

where Ψ_{HY} is the wave function of the hypernuclear state and $H_{i,j}$ means the two-body interaction hamiltonian of two baryons. To focus on the ΛN interaction, (A.1) can be rearranged to be

$$E = \left\langle \Psi_{HY} \left| (H_{core} + \sum_{i}^{A-1} H_{\Lambda,i}) \right| \Psi_{HY} \right\rangle. \tag{A.2}$$

$H_{\Lambda,i}$ is the hamiltonian between Λ and a nucleon. The interactions between other nucleons excpet Λ are merged into one H_{core} term. Because the current work treats the p-shell hypernucleus, it is convinient to further clearify $H_{\Lambda,i}$ into

$$H_{\Lambda,i} = -\frac{\hbar^2}{2m}\Delta_\Lambda(\mathbf{r_\Lambda}) + V_{\Lambda\text{-}\alpha}(\mathbf{r_\Lambda} - \mathbf{r_\alpha}) + \sum_{i=1}^{A-5} V_{\Lambda N_i}(\mathbf{r_\Lambda} - \mathbf{r_{N_i}}). \tag{A.3}$$

Here, $V_{\Lambda\text{-}\alpha}$ is the potential between α, namely nucleons in the s-orbit are coupled to $L = 0$ and $S = 0$, and a Λ in the s-orbit ($s_N s_\Lambda$). $V_{\Lambda N_i}$ is the potential between i-th nucleon in the p-orbit and a Λ ($p_{N_i} s_\Lambda$). This term is expressed using the ΛN effective interaction potential given in Eq. (1.1) as

$$\sum_{i}^{A-5} V_{\Lambda N_i}(\mathbf{r_\Lambda} - \mathbf{r_{N_i}}) = (A-5)\cdot V_0(r) + V_\sigma(r)\sum_{N}^{A-5} \mathbf{s_N}\cdot\mathbf{s_\Lambda} + V_N(r)\sum_{N}^{A-5} \mathbf{l_{N\Lambda}}\cdot\mathbf{s_N}$$
$$+V_\Lambda(r)\sum_{N}^{A-5} \mathbf{l_{N\Lambda}}\cdot\mathbf{s_\Lambda} + V_T(r)\sum_{N}^{A-5} \mathbf{S_{N\Lambda}}. \tag{A.4}$$

Consequently, the wave function, Ψ_{HY}, is divided into the *core*, $s_N s_\Lambda$ and $p_N s_\Lambda$ part. The expression using relative wave function between the nucleon and the Λ ($\phi_{\Lambda N}$) is:

$$\begin{aligned}\Psi_{HY}(\mathbf{r_1}, \mathbf{r_2}, \ldots, \mathbf{r_{A-1}}, \mathbf{r_\Lambda}) &= \prod_{i,j}^{A-1} \phi_{N_iN_j}(\mathbf{r_i} - \mathbf{r_j}) \cdot \prod_{i}^{A-1} \phi_{\Lambda N_i}(\mathbf{r_i} - \mathbf{r_\Lambda}) \\ &= \Psi_{core}(\mathbf{r_1}, \mathbf{r_2}, \ldots, \mathbf{r_{A-1}}) \cdot \underbrace{\prod_{i}^{4} \phi^s_{\Lambda N_i}(\mathbf{r_i} - \mathbf{r_\Lambda})}_{s_N s_\Lambda} \cdot \underbrace{\prod_{i}^{A-5} \phi^p_{\Lambda N_i}(\mathbf{r_i} - \mathbf{r_\Lambda})}_{p_N s_\Lambda},\end{aligned} \tag{A.5}$$

where $\phi^s_{\Lambda N_i}$ and $\phi^p_{\Lambda N_i}$ represent the relative wave functions between the Λ and a nucleon in the s and p orbit, respectively. Since the spatial components of the matrix elements are considered to be the same for any combination of $p_N s_\Lambda$, the strengths of the interaction are expressed in terms of five parameters ($\overline{V}$, Δ, S_N, S_Λ and T).

As an example, some terms that contribute the ground state doublet spacing of ${}^{12}_{\Lambda}$C will be calculated. The configuration of ${}^{12}_{\Lambda}$C is shown in Fig. A.1. The ^{11}C, the *core*, interacts with Λ as a whole without changing the structure of the core state, which is known as weak coupling scheme. Then the ground state of ^{1}1C ($\frac{3}{2}^-$) splits into two levels depends on the Λ spin direction. The Δ term can be calculated from Eq. (1.1) as

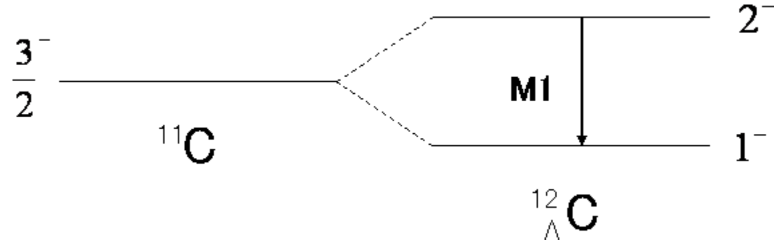

Figure A.1: Ground state doublet configuration in ${}^{12}_{\Lambda}$C

$$\begin{aligned}E_\Delta &= \langle \Psi_{HY} \left| H_{core} + H_{\Lambda,i} \right| \Psi_{HY} \rangle \\ &= \left\langle \Psi_{HY} \left| H_{core} - \frac{\hbar^2}{2m}\Delta_\Lambda(\mathbf{r_\Lambda}) + V_{\Lambda\text{-}\alpha}(\mathbf{r_\Lambda} - \mathbf{r_\alpha}) + \sum_{i=1}^{A-5} V_{\Lambda N_i}(\mathbf{r_\Lambda} - \mathbf{r_{N_i}}) \right| \Psi_{HY} \right\rangle \\ &= \left\langle \Psi_{HY} \left| V_\sigma(r) \sum_{N}^{A-5} \mathbf{s_N} \cdot \mathbf{s_\Lambda} \right| \Psi_{HY} \right\rangle + \text{other}^1 \\ &= \langle J | \mathbf{S_c} \cdot \mathbf{s_\Lambda} | J \rangle \cdot \Delta + \text{other} \\ &= \frac{1}{2} \langle J | (\mathbf{S_c} + \mathbf{s_\Lambda})^2 - \mathbf{S_c}^2 - \mathbf{s_\Lambda}^2 | J \rangle \cdot \Delta + \text{other}\end{aligned} \tag{A.6}$$

Here, J is the total angular momentum of the whole hypernucleus, S_c is the spin of the core nucleus and s_Λ is the spin of the Λ. The total angular momentum of the core, $|J_c\rangle = \sum_{L_c,S_c} C_{L_c,S_c}|J_c; L_cS_c\rangle$, is a good quantum number within jj coupling scheme but $S_c + s_\Lambda$ is not. In this case, $|J\rangle$ has to be decomposed into eigenfunctions of $S_c + s_\Lambda$ using Racah coefficients. $|J\rangle$ is expressed in terms of $6j$-symbols as

$$|J\rangle = \sum_{J'}(-1)^{L_c+S_c+S_\Lambda+J}\sqrt{(2J_c+1)(2J'+1)}\begin{Bmatrix} L_c & S_c & J_c \\ s_\Lambda & J & J' \end{Bmatrix}|(S_cs_\Lambda)J', L_c; J\rangle, \tag{A.7}$$

where $J_c = L_c \otimes S_c$, $J' = S_c \otimes s_\Lambda$ and $J = L_c \otimes S_c \otimes s_\Lambda$. The the contribution to the spacing from the Δ term can be written as

$$\begin{aligned} E_\Delta(2^-) - E_\Delta(1^-) &= \frac{1}{2}(\langle 2|(S_c + s_\Lambda)^2|2\rangle - \langle 1|(S_c + s_\Lambda)^2|1\rangle) \cdot \Delta \\ &= \frac{1}{2}(\underbrace{1 \cdot (1+1)}_{J=2} - \underbrace{\frac{1}{3} \cdot 1 \cdot (1+1) - \frac{2}{3} \cdot 0 \cdot (0+1)}_{J=1}) \cdot \Delta \\ &= \frac{2}{3}\Delta. \end{aligned} \tag{A.8}$$

Similialy, the S_Λ term can be obtained by

$$\begin{aligned} E_{S_\Lambda} &= \left\langle \Psi_{HY} \middle| V_\Lambda(r) \sum_N^{A-5} \mathbf{l_{N\Lambda}} \cdot \mathbf{s_\Lambda} \middle| \Psi_{HY} \right\rangle \\ &= \langle J|\mathbf{l_{N\Lambda}} \cdot \mathbf{s_\Lambda}|J\rangle \cdot S_\Lambda + \text{other} \\ &= \frac{1}{2}\langle J|(\mathbf{l_{N\Lambda}} + \mathbf{s_\Lambda})^2 - \mathbf{l_{N\Lambda}}^2 - \mathbf{s_\Lambda}^2|J\rangle \cdot S_\Lambda + \text{other} \end{aligned} \tag{A.9}$$

Similiar to the case of Δ, the $l_{N\Lambda}+s_\Lambda$ is not a conserved quantity. The $|J\rangle$=$|J_c, s_\Lambda\rangle$ need to be decomposed into the eigenstates of $J' = l_{N\Lambda} \otimes s_\Lambda = L_c \otimes s_N$. The corresponding Racah coefficients can be expressed as

$$|J\rangle = \sum_{J'}(-1)^{L_c+S_c+S_\Lambda+J}\sqrt{(2J_c+1)(2J'+1)}\begin{Bmatrix} S_c & L_c & J_c \\ s_\Lambda & J & J' \end{Bmatrix}|(L_cs_\Lambda)J', s_c; J\rangle, \tag{A.10}$$

The result is

$$\begin{aligned} E_{S_\Lambda}(2^-) - E_{S_\Lambda}(1^-) &= \frac{1}{2}(\langle 2|(l_{N\Lambda} + s_\Lambda)^2|2\rangle - \langle 1|(l_{N\Lambda} + s_\Lambda)^2|1\rangle) \cdot S_\Lambda \\ &= \frac{1}{2}(\underbrace{\frac{3}{2} \cdot (\frac{3}{2}+1)}_{J=2} - \underbrace{\frac{8}{9} \cdot \frac{1}{2} \cdot (\frac{1}{2}+1) - \frac{1}{9} \cdot \frac{3}{2} \cdot (\frac{3}{2}+1)}_{J=1}) \cdot S_\Lambda \\ &= \frac{4}{3}S_\Lambda. \end{aligned} \tag{A.11}$$

Millener claculated in a more sophisticated method based on a shell model for $s^4p^{A-5}s_\Lambda$ configuration. The above results were modified to be 0.47Δ and $1.51S_\Lambda$, respectively.